nature medicine

Implant-derived magnesium induces local neuronal production of CGRP to improve bone-fracture healing in rats

Yifeng Zhang[1,13,14], Jiankun Xu[1,14], Ye Chun Ruan[2,14], Mei Kuen Yu[2], Micheal O'Laughlin[1], Helen Wise[3], Di Chen[4], Li Tian[1], Dufang Shi[1], Jiali Wang[1], Sihui Chen[1], Jian Q Feng[5], Dick Ho Kiu Chow[1], Xinhui Xie[1], Lizhen Zheng[1], Le Huang[1], Shuo Huang[1], Kwoksui Leung[1], Na Lu[6], Lan Zhao[4], Huafang Li[1], Dewei Zhao[7], Xia Guo[8], Kaiming Chan[1], Frank Witte[9,10], Hsiao Chang Chan[2], Yufeng Zheng[11] & Ling Qin[1,12]

Orthopedic implants containing biodegradable magnesium have been used for fracture repair with considerable efficacy; however, the underlying mechanisms by which these implants improve fracture healing remain elusive. Here we show the formation of abundant new bone at peripheral cortical sites after intramedullary implantation of a pin containing ultrapure magnesium into the intact distal femur in rats. This response was accompanied by substantial increases of neuronal calcitonin gene-related polypeptide-α (CGRP) in both the peripheral cortex of the femur and the ipsilateral dorsal root ganglia (DRG). Surgical removal of the periosteum, capsaicin denervation of sensory nerves or knockdown *in vivo* of the CGRP-receptor-encoding genes *Calcrl* or *Ramp1* substantially reversed the magnesium-induced osteogenesis that we observed in this model. Overexpression of these genes, however, enhanced magnesium-induced osteogenesis. We further found that an elevation of extracellular magnesium induces magnesium transporter 1 (MAGT1)-dependent and transient receptor potential cation channel, subfamily M, member 7 (TRPM7)-dependent magnesium entry, as well as an increase in intracellular adenosine triphosphate (ATP) and the accumulation of terminal synaptic vesicles in isolated rat DRG neurons. In isolated rat periosteum-derived stem cells, CGRP induces CALCRL- and RAMP1-dependent activation of cAMP-responsive element binding protein 1 (CREB1) and SP7 (also known as osterix), and thus enhances osteogenic differentiation of these stem cells. Furthermore, we have developed an innovative, magnesium-containing intramedullary nail that facilitates femur fracture repair in rats with ovariectomy-induced osteoporosis. Taken together, these findings reveal a previously undefined role of magnesium in promoting CGRP-mediated osteogenic differentiation, which suggests the therapeutic potential of this ion in orthopedics.

The incidence of trauma-, sports- and age-related musculoskeletal injuries have dramatically increased in recent years, causing extensive medical and socioeconomic burdens[1]. Conventional orthopedic implants made of permanent rigid metals (such as stainless steel or titanium) remove mechanical stress normally loaded onto the bone, known as 'stress shielding,' which precludes load-stimulated bone remodeling and results in gradual bone loss, thus retarding bone-fracture healing[2]. Biodegradable metals, which corrode gradually *in vivo* during the bone-healing process and release corrosion products beneficial to this process, are thought to be more desirable orthopedic implants because they avoid implant-removal surgery and its associated complications (such as refracture and infections)[3].

Magnesium is an essential element that is crucial for bone health[4,5], and ~60% of magnesium in the human body is stored in the bone matrix[6]. Magnesium deficiency leads to osteoporosis, and its supplementation is known to be beneficial to patients with osteoporosis[7]. Possessing a mechanical property similar to that of natural bone, as well as greater stiffness than ceramic biomaterials[6,8], magnesium is considered to be a potential, biodegradable orthopedic implant for the fixation of bone fractures and pseudoarthosis[9]. Pure magnesium, however, is quickly degraded *in vivo* and does not provide prolonged mechanical support for fracture healing. We and other groups have developed magnesium-based alloys or bulk metallic glasses (BMGs), which indeed have shown promising osteogenic effects during

[1]Musculoskeletal Research Laboratory, Department of Orthopedics & Traumatology, The Chinese University of Hong Kong, Hong Kong, PR China. [2]Epithelial Cell Biology Research Centre, School of Biomedical Sciences, Faculty of Medicine, The Chinese University of Hong Kong, Hong Kong, PR China. [3]School of Biomedical Sciences, Faculty of Medicine, The Chinese University of Hong Kong, Hong Kong, PR China. [4]Department of Biochemistry, Rush University, Chicago, USA. [5]Department of Biomedical Sciences, Baylor College of Dentistry, Texas A&M Health Science Center, Dallas, Texas, USA. [6]Division of Life Science, The Hong Kong University of Science and Technology, Kowloon, Hong Kong, PR China. [7]Department of Orthopedics, Dalian University Zhongshan Hospital, Dalian, PR China. [8]Department of Rehabilitation Sciences, The Hong Kong Polytechnic University, Hong Kong, PR China. [9]Julius Wolff Institute and Center for Musculoskeletal Surgery, Charité—Universitätsmedizin Berlin, Berlin, Germany. [10]Berlin-Brandenburg Center for Regenerative Therapies, Charité—Universitätsmedizin Berlin, Berlin, Germany. [11]Department of Materials Science and Engineering, College of Engineering, Peking University, Beijing, PR China. [12]Translational Medicine Research & Development Center, Institute of Biomedical and Health Engineering, Shenzhen Institute of Advanced Technology, Shenzhen, PR China. [13]Present address: Department of Sports Medicine and Adult Reconstructive Surgery, Drum Tower Hospital, School of Medicine, Nanjing University, Nanjing, Jiangsu, PR China. [14]These authors contributed equally to this work. Correspondence should be addressed to L.Q. (lingqin@cuhk.edu.hk) or Y.Z. (yfzheng@pku.edu.cn).

Received 5 January; accepted 13 July; published online 29 August 2016; doi:10.1038/nm.4162

bone-fracture healing[3,8,10–13]. These alloys or BMGs, composed of magnesium, calcium, zinc and strontium, have good corrosion resistance—and thus presumably minor hydrogen production—after implantation into the bone[3,14]. However, whether magnesium actively contributes to the observed osteogenic effects of these alloys or BMGs remains unclear because other composited elements (such as strontium) are also reported to promote bone formation[15,16]. Therefore, in the present study, we used ultrapure magnesium and investigated its possible effects on bone formation, as well as the underlying molecular mechanism.

In long bones, the periosteum, a connective tissue membrane covering the outer surface of bone, has been shown to be important to the integrity, modeling and remodeling of bone, particularly during fracture repair[17], because a large number of mesenchymal stem cells essential for osteogenesis are from the cambium layer of the periosteum. These cells are known as periosteum-derived stem cells (PDSCs)[18]. In addition, the periosteum contains sensory nerves that release neuropeptides known to be involved in osteogenesis[19,20]. Among them, CGRP is suggested to be the most important osteoanabolic peptide[21]. Of note, our previous studies have shown that the implantation of magnesium-based alloys or BMGs into the distal femur in rodents gives rise to increased cortical-bone thickness, with new bone formed at the peripheral cortex next to the periosteum[3,10,12]. We therefore speculated that magnesium might be released from the intramedullary implant into the periosteum, and that PDSCs and sensory nerves in the periosteum might have a role in magnesium-induced bone formation.

To provide magnesium implants with sustained mechanical strength for the fixation and healing of long-bone fractures, we also developed an innovative intramedullary nail (IMN) containing magnesium (Mg-IMN) and investigated its effect on fracture healing in rats with ovariectomy-induced osteoporosis.

RESULTS

Role of the periosteum in magnesium-induced bone formation

We first used a nonfractured femur model to confirm the osteogenic effect of magnesium. We surgically implanted either a 99.99%-pure magnesium rod or, as a control, a stainless steel rod into the medullary cavity of the intact femur in rats. At week 2 after surgery, μX-ray fluorescence (**Supplementary Fig. 1a–d**) and scanning electron microscopy (**Supplementary Fig. 1e–h**) revealed a remarkably higher magnesium concentration in the cortical bone and bone–periosteum junction of the magnesium-implanted femora, as compared to that of the controls, which suggests the diffusion of magnesium from the implant across the bone toward the periosteum. Meanwhile, H&E staining and calcein labeling showed a substantially larger amount of new bone formation, mainly at the peripheral cortex, in magnesium-implanted femora, as compared to the controls (**Fig. 1a**). Micro-computed tomography (CT) measurements confirmed significantly higher total bone tissue volume (TV), high-density bone volume (BV) and ρ-moment of inertia (ρMOI) in magnesium-implanted femora, as compared to that in controls (**Fig. 1b**,**c**).

To evaluate the role of the periosteum in magnesium-induced new-bone formation, we surgically removed the periosteum when magnesium rods were implanted. As a result, new bone was no longer formed at regions where the periosteum had been removed successfully, and was instead found only at peripheral cortex that contained residual periosteum, as shown by both radiographs and micro-CT (**Fig. 1b**,**c** and **Supplementary Fig. 2a**).

CGRP is involved in magnesium-induced bone formation

To test the possible role of sensory nerves in the periosteum in the osteogenic effect of magnesium, we destroyed the sensory nerves by injecting high-dose capsaicin into the dorsal spine in rats, as previously reported[22]. Consequently, the degree of magnesium-induced new-bone formation was significantly lower than that in the group without capsaicin treatment (**Fig. 1d**,**e**). Moreover, similarly to the effect of implanted magnesium rods, the injection of $MgCl_2$ (10 mM in a volume of 100 μl, daily for 3 d) directly at one side of the L3–L5 lumbar spine also induced new bone formation at the peripheral cortex of the ipsilateral femur (**Supplementary Fig. 2b**). In magnesium-implanted femora at week 2 after surgery, immunofluorescence staining showed abundant CGRP in peripheral cortical bone, whereas in controls, only scattered CGRP labeling was found (**Fig. 1f**). ELISA analysis showed that the concentration of CGRP in bone tissues was higher after magnesium implantation, which peaked at day 4 with a value eight-fold higher than the controls, and was lower at day 7 and 14, as compared to day 4, but the values were still two-fold higher than the controls (**Fig. 1f**). In addition, at week 2 after surgery, substantially higher expression of CGRP was also found in L4 DRGs in rats with magnesium implantation, as compared to the controls (**Fig. 1g**).

We also measured the concentrations of other sensory neuropeptides, including substance P, neurokinins and galanin, in implanted femora, given that beneficial effects on bone healing have also been reported for these[23,24]. ELISA analysis showed that the concentration of substance P was higher by approximately one-fold at day 4, whereas neurokinin K and galanin were not notably different after magnesium implantation, as compared to the control group (**Supplementary Fig. 2c**). These results suggest that CGRP might be the predominant neuropeptide contributing to magnesium-induced bone formation. To test this idea, we injected BIBN4096BS (BIBN, 750 μg/ml in a volume of 100 μl, every other day), a CGRP-receptor antagonist, into rat femora in conjunction with magnesium implantation, which resulted in substantially lower TV and BV values in magnesium-implanted femora than in the non-BIBN-treated group (**Supplementary Fig. 2d–f**).

To further confirm the involvement of CGRP and its receptor in magnesium-induced osteogenesis, we injected complementary DNA (cDNA)-conjugated and short interfering RNA (shRNA)-conjugated adenovirus to overexpress or knockdown calcitonin receptor–like receptor (*Calcrl*) or receptor activity-modifying protein 1 (*Ramp1*, the direct binding site for CGRP) in rat femur *in vivo* (**Supplementary Fig. 3**). An *in vivo* imaging system revealed that fluorescent adenoviruses conjugated with *Calcrl* (AdV-*Calcrl*) or shRNA targeting *Calcrl* (AdV-sh*Calcrl*) were located at the injected femur with some diffusion to the contralateral femur, yet were undetectable in major metabolic organs (**Supplementary Fig. 3a**). PCR and western blot assays confirmed successful overexpression or knockdown of *Calcrl* or *Ramp1* in the femora (**Supplementary Fig. 3b**,**c**). As shown by radiographs (**Fig. 2a**) and calcein/xylenol double labeling (**Fig. 2b**), *Calcrl* overexpression by AdV-*Calcrl* further enhanced magnesium-induced new-bone formation, whereas its knockdown by AdV-sh*Calcrl* attenuated this process. According to micro-CT analysis, significantly greater TV and BV, with no difference in BV/TV or bone mineral density (BMD), were observed in magnesium-implanted femora in conjunction with *Calcrl* overexpression by AdV-*Calcrl*, as compared to the magnesium-implanted femora treated with scrambled adenoviruses as a negative control (AdV-NC) (**Fig. 2c**). Conversely, significantly lower TV was found in the AdV-sh*Calcrl*-treated and magnesium-implanted femora than in the

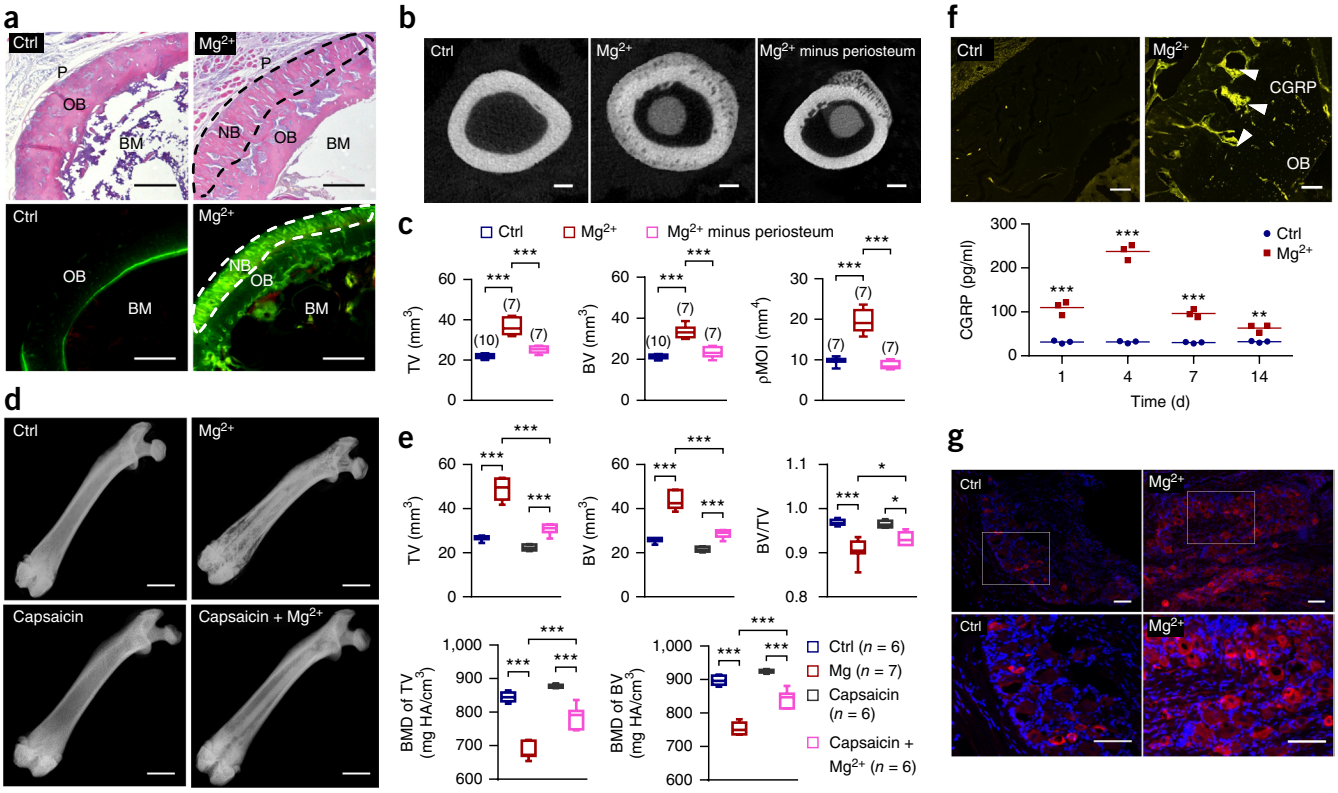

Figure 1 Periosteum-dependent new-bone formation induced by magnesium in rat femur. (**a**) Representative H&E staining (top) and calcein-green labeling (bottom) for new bone in the mid-shaft of rat femora intramedullary implanted with a magnesium (Mg^{2+}) or stainless steel (as control (Ctrl)) rod for 2 weeks ($n = 6$ images per group). P, periosteum; BM, bone marrow; OB, old bone; NB, new bone. Scale bars, 200 μm. (**b**,**c**) Representative micro-CT images (**b**, $n \geq 7$ images per group) and corresponding measurements (**c**) of total bone TV, high-density BV and ρMOI in rat femora implanted with Mg^{2+} or Ctrl rods, or denuded of the periosteum with magnesium implantation (Mg^{2+} minus periosteum). $^{***}P < 0.001$ by one-way ANOVA with Tukey's *post hoc* test. Parenthetic numbers indicate *n* value for each group. Scale bars, 1 mm. Stainless-steel implants were removed from the bone before micro-CT to avoid scanning artifact. (**d**,**e**) Representative radiographs (**d**, $n \geq 6$ images per group) and micro-CT measurements of TV, BV and BMD (**e**) in rat femora 2 weeks after Mg^{2+} or Ctrl implantation with or without capsaicin treatment (see Online Methods). $^{*}P < 0.05$, $^{***}P < 0.001$ by one-way ANOVA with Tukey's *post hoc* test. *n* is shown for each group in parentheses. Scale bars, 5 mm. mg HA/cm^3, unit of hydroxyapatite density. (**f**) Representative immunofluorescence labeling (top, $n = 1$ image from each of three rats per group used) and ELISA analysis (bottom) for CGRP in rat femora 2 weeks after implantation. Arrowheads indicate CGRP-positive area. $^{**}P < 0.01$, $^{***}P < 0.001$ by two-way ANOVA with Bonferroni *post hoc* test, $n = 3$ biological replicates. Scale bars, 50 μm. (**g**) Representative images of immunofluorescence staining ($n = 1$ image from each of three rats per group used) for CGRP in DRGs in L4 lumbar from rats at 2 weeks after implantation. Lower images are high-resolution versions of the boxed regions in the upper images. Nuclei are labeled with DAPI. Scale bars, 50 μm. Data throughout are means ± s.e.m.

magnesium-implanted femora co-treated with AdV-NC (**Fig. 2c**). Furthermore, we observed substantially greater amounts of calcein-labeled new bone and significantly higher TV and BV in magnesium-implanted femora with *Ramp1*-overexpression by AdV-*Ramp1*, whereas we observed less calcein-labeling with significantly lower TV and BV in those with *Ramp1*-knockdown by AdV-sh*Ramp1*, as compared to the magnesium-implanted femora treated with AdV-NC. (**Fig. 2d**,**e**).

CGRP is encapsulated by synaptic vesicles and released from the axon terminals of DRG neurons[25,26]. Thus, we evaluated the effect of magnesium on synaptic-vesicle aggregation in DRG neurons isolated from rats (**Fig. 3a**). Immunofluorescence labeling revealed CGRP expression in isolated DRG neurons (**Fig. 3b**). The synaptic vesicles in the DRG neurons were labeled with a fluorescent dye, FM1-43, and monitored with a live-cell confocal system. In the absence of magnesium ions (Mg^{2+}) in the bath, FM1-43-labeled vesicles were seen mainly in neuron bodies. Upon the addition of $MgCl_2$ (1 mM) into the bath, FM1-43 intensity at neuronal terminals was increased within 5 min. Subsequently, another 1 mM $MgCl_2$ was added to reach an accumulative concentration of 2 mM, which induced further increase in FM1-43 intensity at neuronal terminals (**Fig. 3c** and **Supplementary Video 1**), and thus suggests that Mg^{2+} induces the movement and aggregation of these vesicles toward neuronal terminals. Because *N*-methyl-D-glucamin (NMDG) is a cell-membrane nonpermeable cation, NMDG-Cl was added as a control, which induced no obvious effect on FM1-43 intensity at neuronal terminals, excluding the involvement of Cl^- in this process (**Supplementary Fig. 4a**). In addition, Zn^{2+} and Mn^{2+}, two divalent cations similar to Mg^{2+}, inhibited, rather than promoted, FM1-43-labeled vesicle aggregation (**Supplementary Fig. 4b**,**c**). Moreover, the effect of Mg^{2+} on vesicle aggregation was abolished in cells pretreated with cytochalasin B (**Fig. 3d**), which inhibits actin polymerization[27]. In addition, the intracellular ATP concentration was elevated after treating the isolated DRG neurons with Mg^{2+} (**Fig. 3e**). These results therefore suggest that Mg^{2+} might promote synaptic-vesicle aggregation by enhancing ATP-facilitated actin polymerization.

To examine whether Mg^{2+} could enter DRG neurons, we used a Mg^{2+} sensitive dye, Mg-Fura2, to monitor intracellular Mg^{2+}

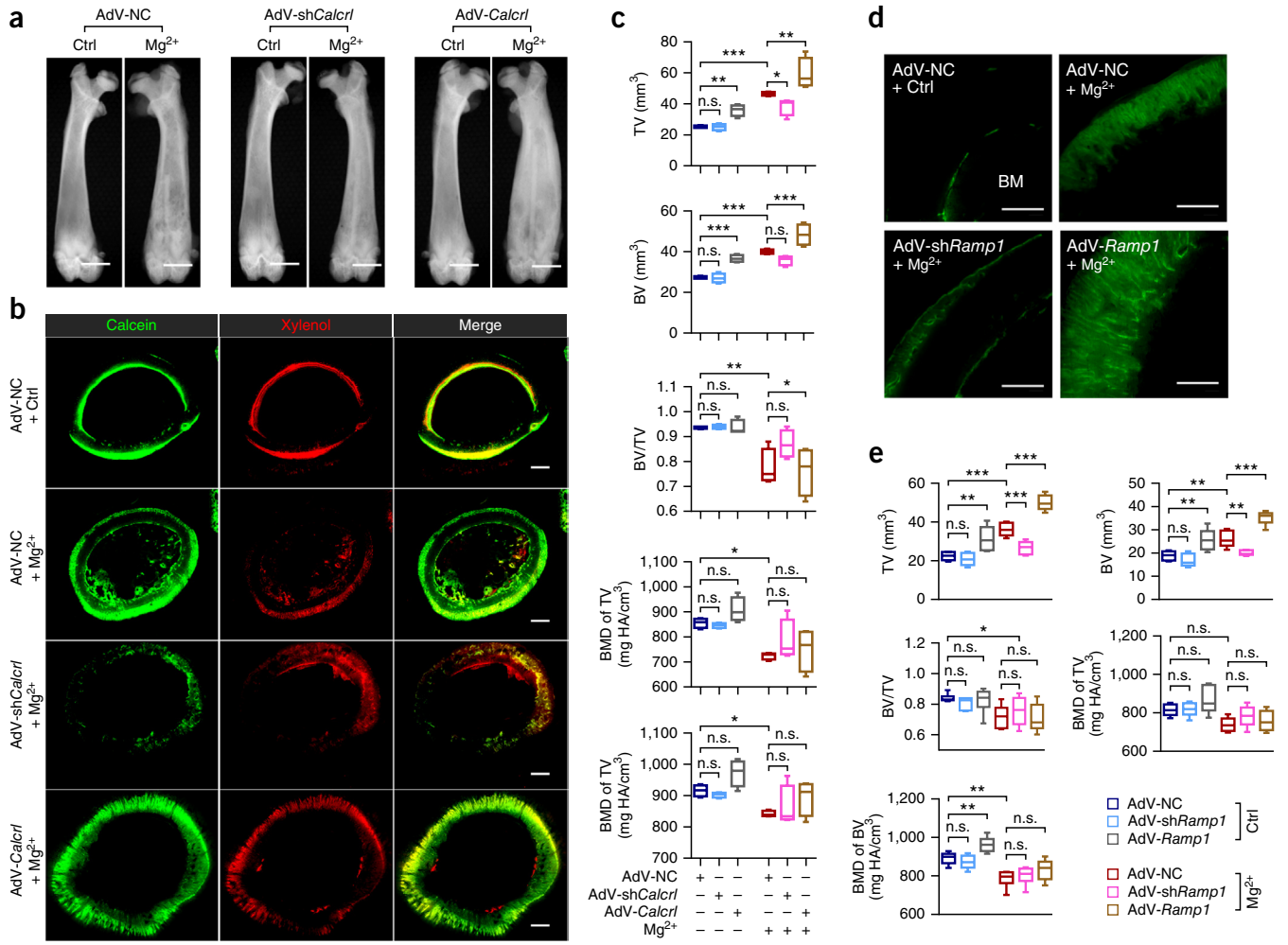

Figure 2 Role of CGRP receptor in magnesium-induced new-bone formation in rat femur. (**a**–**c**) Representative radiographs (**a**, $n = 1$ image from each of four rats per group used), calcein/xylenol assessment of bone remodeling (**b**, $n = 1$ image from each of four rats per group used) and micro-CT measurements of BV, TV and BMD (**c**) in rat femora 2 weeks after Mg^{2+} or Ctrl implantation, with pretreatment with adenoviruses conjugated with *Calcrl* cDNA (AdV-*Calcrl*) or shRNA targeting *Calcrl* (AdV-sh*Calcrl*) to overexpress or knockdown *Calcrl*, respectively. Adenovirus with scrambled sequence was used as the negative control (AdV-NC). $^*P < 0.05$, $^{**}P < 0.01$, $^{***}P < 0.001$, n.s., $P > 0.05$ by one-way ANOVA with Newman–Keuls *post hoc* test. $n = 4$ animals per group. Scale bars, 5 mm (**a**) and 1 mm (**b**). (**d**,**e**) Representative calcein-green labeling for new bone (**d**, $n = 6$ images per group) and micro-CT measurements of BV, TV and BMD (**e**) in rat femora 2 weeks after Mg^{2+} or Ctrl implantation with the pretreatment of adenoviruses conjugated with *Ramp1* cDNA (AdV-*Ramp1*), shRNA targeting *Ramp1* (AdV-sh*Ramp1*) or AdV-NC, respectively. $^*P < 0.05$, $^{**}P < 0.01$, $^{***}P < 0.001$, n.s., $P > 0.05$ by one-way ANOVA with Newman–Keuls *post hoc* test. $n = 6$ animals per group. Scale bars, 500 μm (**d**). Data throughout are means ± s.e.m.

concentration ($[Mg^{2+}]i$) changes in DRG neurons. The results showed that the addition of $MgCl_2$ (10 mM) into the Mg^{2+}-free bath induced a notable increase in $[Mg^{2+}]i$, indicating the entry of Mg^{2+} into DRG neurons. Given that TRPM6, TRPM7 and MAGT1 are reported to transport Mg^{2+} across cell membranes[28,29], we also examined the effects of their blockers (**Fig. 3f**). The results showed that Mg^{2+}-entry was significantly inhibited by nitrendipine (50 μM, inhibiting MAGT1 (ref. 30)) or 2-aminoethoxydiphenyl borate (2-APB) (100 μM, inhibiting TRPM7 (ref. 31)), but not by ruthenium red (50 μM, inhibiting TRPM6 (ref. 32)).

CGRP promotes the osteogenic differentiation of PDSCs

In magnesium-implanted femora, we detected numerous cells at the region between the periosteum and newly formed bone (**Fig. 4a**), which are presumably PDSCs. We isolated the cells from the periosteum of rat femora, and they were positively labeled with stem cell markers (**Supplementary Fig. 5**), which suggests that they are PDSCs. Consistently with results *in vivo*, alkaline phosphatase (ALP) and alizarin red (AR) staining showed greater osteogenic differentiation capacity of PDSCs isolated from magnesium-implanted rat femora, as compared to those from stainless-steel-implanted (as control, Ctrl) or nonimplanted (as blank control, Blk) femora (**Fig. 4b**). To verify a role for CGRP in the mediation of magnesium-induced osteogenesis, we examined the effects of CGRP on isolated PDSCs. First, no increase in the proliferation of PDSCs by CGRP (up to 10^{-8} M) was observed (**Fig. 4c**). We next induced osteogenic differentiation of PDSCs in the presence of CGRP. Real-time PCR results showed that the treatment of PDSCs with CGRP (10^{-12}–10^{-8} M) for 2 weeks significantly promoted transcription of the osteogenic markers *Alp*, *Bglap* and *Opn* in a concentration-dependent manner (**Fig. 4d**). As shown by ALP and AR staining, the CGRP-induced osteogenic differentiation of PDSCs was promoted by AdV-based overexpression of *Calcrl* or *Ramp1* and diminished by their knockdown (**Fig. 4e** and **Supplementary Fig. 3d**).

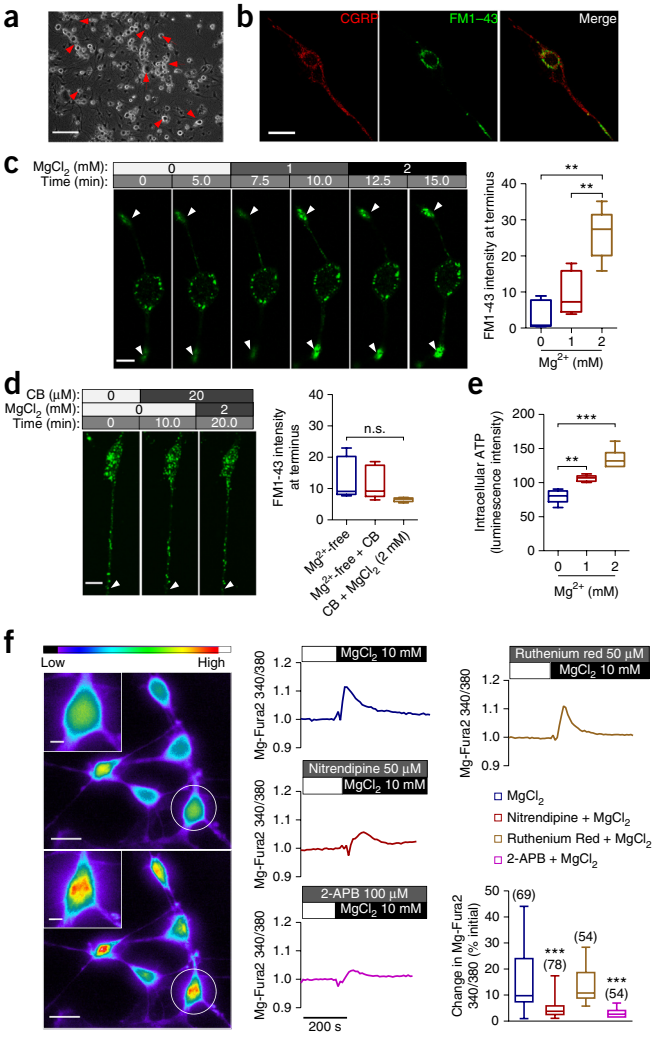

Figure 3 Effect of Mg^{2+} on rat DRG neurons *in vitro*. (**a**) Representative bright-field photograph of DRG neurons isolated from rats ($n = 10$ images). Arrows indicate large phase-bright DRG neurons. Scale bar, 100 μm. (**b**) Fluorescence labeling for CGRP (red) and neuronal vesicles with FM1-43 (green) in cultured DRG neurons. Scale bar, 20 μm. (**c**) Confocal live-cell imaging (left) of DRG neurons pre-loaded with FM1-43 in Mg^{2+}-free bath (at 0 and 5 min) and after the addition of $MgCl_2$ (1–2 mM) (at 7.5, 10, 12.5 and 15 min). Arrowheads indicate neuronal terminus. Corresponding quantification (right) of FM1-43 intensity at neuronal terminus. $^{**}P < 0.01$ by one-way ANOVA with Tukey's *post hoc* test, $n = 5$ cells per group. Scale bar, 10 μm. (**d**) Representative confocal images (left, $n = 5$ images per group) and corresponding quantification (right) of FM1-43-loaded DRG neurons treated with cytochalasin B (CB, 20 μM), an inhibitor of actin polymerization, and subsequently, $MgCl_2$ (2 mM). n.s., $P > 0.05$ by one-way ANOVA with Tukey's *post hoc* test, $n = 5$ cells per group. Scale bar, 10 μm. (**e**) Measurement of intracellular ATP concentration in DRG neurons after incubation with different concentrations of Mg^{2+} for 24 h. $^{**}P < 0.01$, $^{***}P < 0.001$ by one-way ANOVA with Tukey's *post hoc* test, $n = 6$ culture wells of cells for biological replicates. (**f**) Mg-Fura2 detection of Mg^{2+}-entry into DRG neurons. Representative fluorescence photographs (excited at 340 nm) (left) of DRG neurons before (top) and after (bottom) the addition of $MgCl_2$ (10 mM) into Mg^{2+}-free bath ($n \geq 10$ images per condition). Color ranges from low (black to purple) to high (red to white) levels of Mg^{2+}. Insets show high magnification of circled area. Time-course changes (right) in intracellular Mg^{2+} levels (indicated by 340/380 ratio of Mg-Fura2) in DRG neurons in the absence or presence of nitrendipine (50 μM, inhibiting MAGT1), 2-APB (100 μM, inhibiting TRPM7) or ruthenium red (50 μM, inhibiting TRPM6 and TRPV) before and after the addition of $MgCl_2$ (10 mM) into the Mg^{2+}-free buffer. $^{***}P < 0.001$ by one-way ANOVA with Tukey's *post hoc* test; n is shown in parentheses in each column. Scale bars, 20 μm (main images); 5 μm (inserts). Data throughout are means ± s.e.m.

Activation of the CGRP receptor initiates the cyclic adenosine monophosphate (cAMP)-signaling pathway, which can lead to phosphorylation of the transcription factor CREB1 (ref. 33), which subsequently activates Sp7 transcription factor (SP7, also known as Osterix) and runt-related transcription factor 2 (RUNX2), two other transcription factors that are known to be crucial for osteogenesis[34,35]. We therefore examined these transcription factors in CGRP-treated PDSCs. Western blot results showed that treatment with CGRP (10^{-10} M, 72 h) resulted in greater levels of phosphorylated (p) CREB1 and SP7 in PDSCs as compared to those without CGRP treatment, which was blunted by AdV-sh*Calcrl*-induced *Calcrl* knockdown (**Fig. 4f**). No remarkable change in RUNX2 expression was found (**Fig. 4f**).

We also examined the effect of conditioned medium from DRG neuron cultures on the osteogenic differentiation of PDSCs. DRG neurons were cultured in the absence or presence of $MgCl_2$ (2 mM) for 3 d before the conditioned medium was collected. As shown by ALP and AR staining, treating the PDSCs with Mg^{2+}-conditioned, neuronal-culture medium facilitated the cells' osteogenic differentiation, as compared to cells treated with the control medium, and this facilitation was inhibited in cells with *Calcrl* knocked down by AdV-sh*Calcrl* (**Fig. 4g**).

Mg-IMN promotes fracture healing

In spite of the observed osteogenic effects, pure magnesium rods failed to fix long-bone fractures in mice 3 weeks after implantation (**Supplementary Fig. 6a**), probably owing to degradation of the rod and thus deterioration of its mechanical strength over time. To translate the osteogenic effect of magnesium for orthopedic application, we developed a 'bioactive' Mg-IMN by inserting a magnesium rod into a hollow IMN made of stainless steel with holes drilled in the middle of the nail as vents for magnesium release (**Supplementary Fig. 6b,c**). Finite elemental analysis (FEA) of the designed Mg-IMN suggested that its mechanical strength was comparable to that of nondrilled nails (**Supplementary Fig. 6d**).

We then tested the ability of the Mg-IMN system to heal fractured femurs in rats with ovariectomy-induced osteoporosis, as compared to an IMN implant without a magnesium insert. Given the suggested involvement of the periosteum in the beneficial effects of magnesium on fracture healing, we used a closed femora fracture model (see Online Methods) in which the periosteum remained intact during bone injury. We first confirmed diffusion of magnesium from the Mg-IMN system into the bone and the periosteum (**Supplementary Fig. 6e**), as was seen similarly with the use of the pure-magnesium rod in intact femora (**Supplementary Fig. 1**). X-ray analysis showed that at week 4 after implantation, both the width and area of callus in the Mg-IMN-implanted group were significantly larger than those in the IMN group, although no difference between the two groups was found at week 6, 8 or 12 (**Fig. 5a,b**). Micro-CT results showed greater TV and BV, but lower BV/TV, in the Mg-IMN group, as compared to the IMN group, at week 4 (**Fig. 5c** and **Supplementary Fig. 7a**). At later weeks after implantation, the TV of the Mg-IMN group was lower and no longer different than that of the IMN group (**Fig. 5c**). The BV of the Mg-IMN group, however, remained higher than the control group at week 8 after implantation, but by week 12, there was

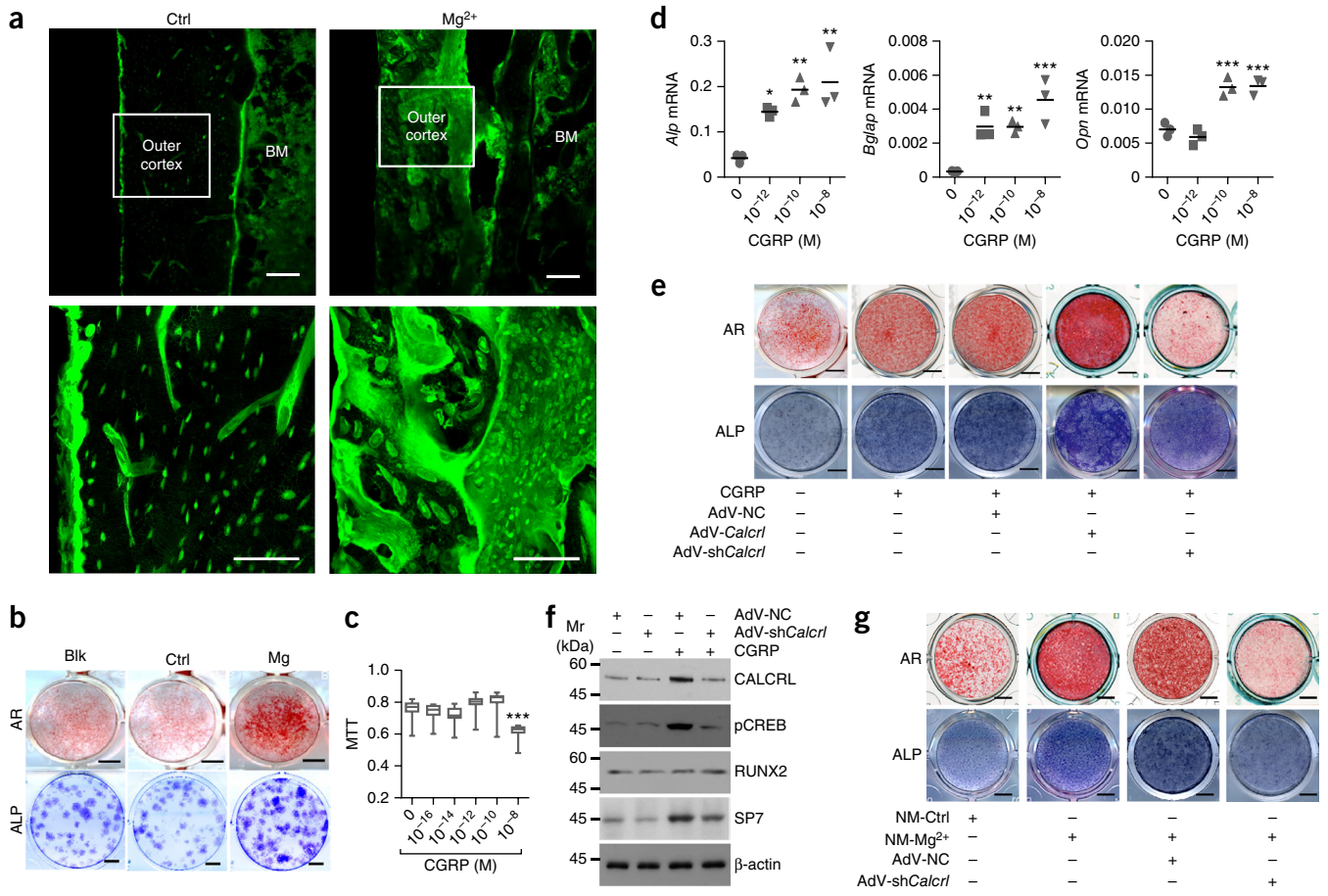

Figure 4 CGRP promotes osteogenic differentiation of periosteum-derived stem cells (PDSCs). (**a**) Confocal images of FITC-labeled peripheral cortex of cortical bone (outer layer) in rat femora implanted for 2 weeks with Mg^{2+} or Ctrl rods ($n = 1$ image from each of four rats used). Scale bars, 100 μm. (**b**) Alizarin red (AR) and alkaline phosphatase (ALP) staining in PDSCs isolated from rat femora implanted for 2 weeks with Mg^{2+} or Ctrl rods, or nonimplanted ones as the blank control (Blk). Scale bars, 5 mm. (**c**) 3-(4,5-dimethylthiazol-2-yl)-2,5-diphenyltetrazolium bromide (MTT) assay of PDSCs isolated from nonimplanted rat femora after 72-h incubation period with CGRP (0–10^{-8} M). (**d**) Real-time PCR analysis of *Alp*, osteocalcin (*Bglap*) and osteopontin (*Opn*) mRNA expression in the PDSCs after a 2-week incubation period with CGRP. In **c**, $n = 8$ biological replicates, and in **d**, $n = 3$ biological replicates. $^*P < 0.05$, $^{**}P < 0.01$ and $^{***}P < 0.001$, as compared to cells in the absence of CGRP, by one-way ANOVA with Dunnett's *post hoc* test. Data are means ± s.e.m. Shapes of circle, square, triangle and del operator represent the addition, respectively, of 0, 10^{-12}, 10^{-10} or 10^{-8} M CGRP. (**e**,**f**) AR and ALP staining (**e**) and representative western blotting ($n = 3$ experiments) for CALCRL, pCREB1, RUNX2 and SP7 (**f**, $n = 3$ western blots per condition) in the PDSCs transfected with (+) or without (–) AdV-*Calcrl*, AdV-sh*Calcrl* or AdV-NC in absence (–) or presence (+) of CGRP (10^{-10} M). Mr, marker. Scale bars, 5 mm. (**g**) ALP and AR staining in the PDSCs after 14-d incubation with condition media, which were collected from DRG neuron cultures in absence (NM-Ctrl) or presence of Mg^{2+} (NM-Mg^{2+}) (see Methods). Scale bars, 5 mm.

no difference in BV between the two groups (**Fig. 5c**). The BMD of TV in the Mg-IMN group was lower at week 4, but higher at week 12, than that of the IMN group (**Fig. 5c**). These results suggested that more callus tissue was formed at the early stage of fracture healing, and that the mineralization process was accelerated at later stages in the Mg-IMN group, as compared to the IMN group. Importantly, a four-point bending biomechanical test at week 12 showed a significantly greater maximum compressive load of the femoral shafts in the Mg-IMN group than in the IMN group (**Fig. 5d**).

Histomorphometric analysis suggested a typical pattern of secondary fracture healing, with callus formation, intramembranous ossification and endochondral ossification identified in all the samples (**Fig. 5e**,**f** and **Supplementary Fig. 7b**). More periosteal woven bone, accompanied by elevated CGRP expression in the callus, at week 2 and more endochondral tissue at week 4 were seen in the Mg-IMN group relative to the IMN group (**Fig. 5e**,**f** and **Supplementary Fig. 7c**). From week 8 to 12, woven bone and endochondral tissue were gradually replaced by lamellar structure bridging the fracture gap (**Supplementary Fig. 7b**). Polarized light images to identify collagen fibers revealed a better alignment of the collagen fibers inside the callus in the Mg-IMN group at week 4, as compared to that in the IMN group (**Fig. 5f**). More bright fibers and regular lamellar bone was found in the Mg-IMN group than in the IMN group, indicating advanced remodeling with better lamellar alignment, and therefore, presenting a superior mechanical property in the Mg-IMN group. Moreover, calcein/xylenol double labeling suggested accelerated new-bone formation in the Mg-IMN group from week 4 to 8, as compared to the IMN group (**Fig. 5g**,**h**). At week 12, the ratio of xylenol/calcein staining of the Mg-IMN group was significantly lower than that of the IMN group, suggesting the formation of mature lamellar bone tissue (**Fig. 5g**,**h**). Consistently with results *in vitro*, the expression of SP7 in facture callus was substantially higher in the Mg-IMN group than in the IMN group, with no difference in RUNX2 expression between the two groups at

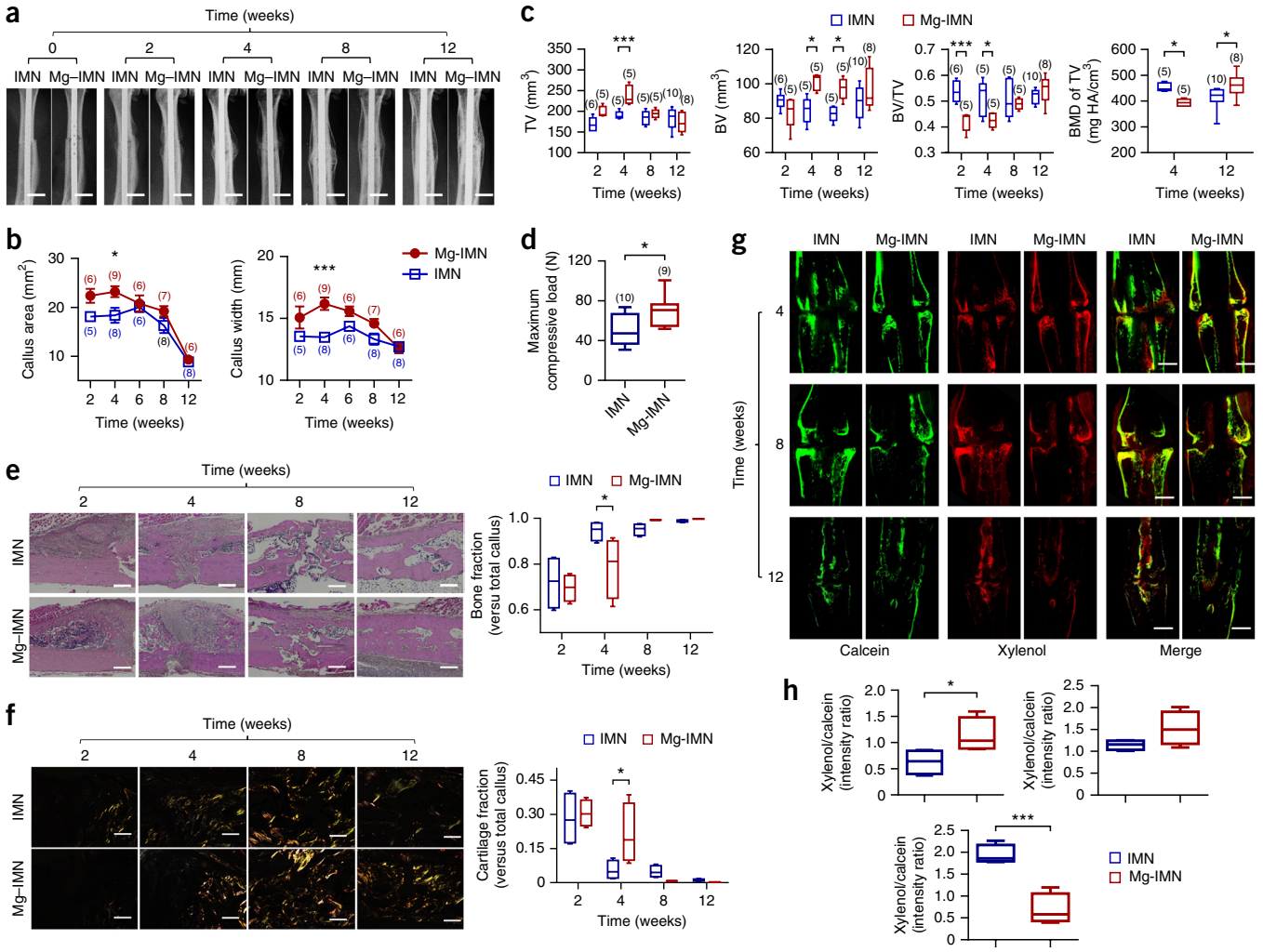

Figure 5 Innovative magnesium-containing intramedullary nail accelerates fracture healing of femoral shaft in rats with ovariectomy-induced osteoporosis. (**a**,**b**) Representative radiographs (**a**, $n \geq 5$ images per group) and quantification of the area and width (**b**) of the fracture callus in rat femora 2–12 weeks after implantation with IMN or Mg-IMN. $^{*}P < 0.05$, $^{***}P < 0.001$ by two-way ANOVA with Bonferroni *post hoc* test. *n* is shown in parentheses for each group. Scale bars, 5 mm. (**c**) Micro-CT measurements of TV, BV, BV/TV and TV density of fractured rat femora 2–12 weeks after IMN or Mg-IMN implantation. $^{*}P < 0.05$, $^{***}P < 0.001$ by two-way ANOVA with Bonferroni *post hoc* test. *n* is shown in parentheses for each group. (**d**) Biomechanical test of maximum compressive load of the fractured rat femora 12 weeks after IMN or Mg-IMN implantation. $^{*}P < 0.05$ by Student's *t* test. *n* is shown in parentheses for each group. (**e**,**f**) Representative images of H&E staining (**e**, $n = 1$ image from each of four rats per group) and polarized light analysis (**f**, $n = 1$ image from each of four rats per group) in mid-sagittal section of the fracture callus 2–12 weeks after implantation of IMN or Mg-IMN with quantitation (right) of bone (**e**) and cartilaginous (**f**) fractions. $n = 4$ animals per group; $^{*}P < 0.05$, by two-way ANOVA with Bonferroni *post hoc* test. Scale bars, 500 µm. (**g**) Bone-remodeling assessment by calcein/xylenol double-labeling ($n = 1$ image from each of four rats per group) in rat femora 4–12 weeks after implantation with IMN or Mg-IMN. Scale bars, 5 mm. (**h**) Rate of bone remodeling is indicated by xylenol/calcein intensity ratios (top, week 4 data; middle, week 8 data; bottom, week 12 data). $n = 4$ samples per group, $^{*}P < 0.05$, $^{***}P < 0.001$ by Student's *t* test. Data are means ± s.e.m.

week 2 (**Supplementary Fig. 7d**). In addition, double staining for the proliferation marker Ki67 and the osteoblast marker RUNX2 showed a significantly ($P < 0.001$) larger number of cells at week 2 expressing both Ki67 and RUNX2 in the fracture callus of the Mg-IMN group than in that of the IMN group (**Supplementary Fig. 7e**). Consistently, in cells of the osteoblast line MC3T3-E1, the addition of CGRP (10^{-10} M) in culture medium promoted greater cell proliferation, as compared to control treatment (**Supplementary Fig. 7f**). Such enhanced proliferation of osteoblasts might underlie the larger callus size observed at an early stage of fracture healing in Mg-IMN-implanted femora (**Fig. 5a**,**b**).

Given that CGRP sensory nerves are associated with pain, we tested pain levels in rats that received implantations by measuring the alternation of gait pattern, using the automated CatWalk system[36,37]. In both IMN and Mg-IMN groups, the limb idleness index (LII) score increased and the print area (at the implanted side) decreased at week 1 after implantation, as compared to that before the surgery, indicating pain (**Supplementary Fig. 8**). However, neither LII nor print area differed between the Mg-IMN and IMN group at weeks 1 and 2 (**Supplementary Fig. 8a**,**b**), which suggests similar gait patterns and pain levels, even though at day 4, CGRP expression was considerably higher in the Mg-IMN group than in the IMN group (**Supplementary Fig. 8c**). Because aberrant sprouting of nerve fibers can also cause pain, we examined the growth of nerve fibers 1–14 d after surgery. The expression of growth-associated protein 43, a marker for newly generated nerves[38], although initially higher at day 4, was significantly

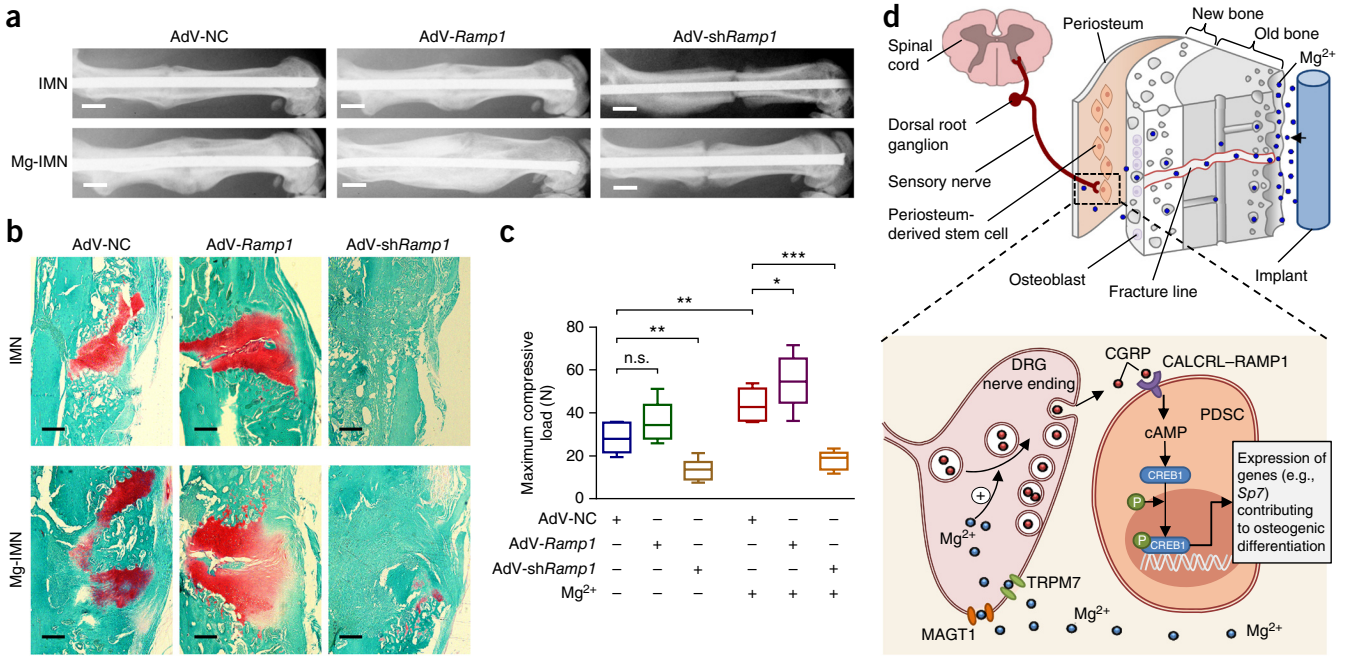

Figure 6 Role of CGRP receptor in the beneficial effect of Mg-IMN on bone-fracture healing in rats. (**a**–**c**) Radiographs (**a**), safranin O staining (**b**) and biomechanical test of maximum compressive load (**c**) of the fractured rat femora 4 weeks after implantation with IMN or Mg-IMN in conjunction with treatment of AdV-NC, AdV-*Ramp1* or AdV-sh*Ramp1*. $n = 6$ animals per group. $^{*}P < 0.05$, $^{**}P < 0.01$, $^{***}P < 0.001$, n.s., $P > 0.05$ by one-way ANOVA with Newman-Keuls *post hoc* test. Data are presented as means ± s.e.m. Scale bars, 5 mm (**a**) and 200 μm (**b**). Images are representative of six images taken from each group. (**d**) Schematic diagram showing diffusion of implant-derived Mg^{2+} across the bone toward the periosteum that is innervated by DRG sensory neurons and enriched with PDSCs undergoing osteogenic differentiation into new bone (top). Inset (shown enlarged at bottom), the released Mg^{2+} enters DRG neurons via Mg^{2+} transporters or channels (i.e., MAGT1 and TRPM7) and promotes CGRP-vesicles accumulation and exocytosis. The DRG-released CGRP, in turn, activates the CGRP receptor (consisting of CALCRL and RAMP1) in PDSCs, which triggers phosphorylation of CREB1 via cAMP and promotes the expression of genes contributing to osteogenic differentiation.

($P < 0.001$) lower at day 7 in the Mg-IMN group than in the IMN group (**Supplementary Fig. 8d**). No difference in protein gene product 9.5, a marker for mature nerves[38], was found between the two groups from day 4 to day 14 (**Supplementary Fig. 8d**).

CGRP receptor mediates Mg-IMN-promoted bone-fracture healing

To confirm the role of CGRP and its receptor in Mg-IMN-facilitated bone-fracture healing, we performed *Ramp1* knockdown and overexpression *in vivo*, in conjunction with Mg-IMN implantation. Radiographs (**Fig. 6a**) and safranin O staining (**Fig. 6b**) showed that Mg-IMN-facilitated bone-fracture healing was further enhanced by AdV-*Ramp1*-induced overexpression and abrogated by AdV-sh*Ramp1*-induced knockdown of *Ramp1*, as compared to co-treatment with a control vector. In addition, aberrant fibrous tissue was found to be filling the fracture gaps in the femora with *Ramp1* knockdown (**Fig. 6b**).

We also performed a four-point bending biomechanical test to determine the strength of the healing fracture in these different treatment groups. We found that the maximum compressive load was significantly lower in AdV-sh*Ramp1*-treated, and higher in AdV-*Ramp1*-treated femora, with Mg-IMN implantation, as compared to those treated with AdV-NC, at week 4 after surgery (**Fig. 6c**).

DISCUSSION

Studies of humans and other species have suggested the potential of magnesium-based alloys or BMG in the promotion of bone formation[3,10,12,39–42], yet the underlying mechanism(s) for this beneficial effect remains unexplained. The present study has provided compelling evidence from findings both *in vitro* and *in vivo* for a contribution of magnesium to the robust promotion of bone formation and enhancement of fracture healing with the underlying mechanisms elucidated. To a great extent, the beneficial effects of magnesium are mediated by CGRP, a neuropeptide released from the sensory neuronal endings in the periosteum of the long-bone shaft. Although it has long been known that the central nervous system has an important role in the regulation of bone formation[43,44], the exact role of sensory nerves in this process has remained elusive. Here a previously unrecognized CGRP-mediated cross-talk pathway between peripheral nerves and PDSCs has been identified as a major mechanism underlying magnesium-induced bone formation (**Fig. 6d**).

A few points from our findings support the involvement of CGRP sensory nerves in the beneficial effects of magnesium. First, magnesium-induced bone formation was largely reduced by destroying the sensory nerves or by removal of the periosteum, where a large number of sensory nerves exist. Second, magnesium induced abundant expression of neuron-derived CGRP in the newly formed bone. Studies on DRG neuronal cultures suggest that such an effect of Mg^{2+} on CGRP occurs through (i) MAGT1- and TRPM7-mediated Mg^{2+}-entry into neurons and (ii) Mg^{2+}-facilitated CGRP-vesicle aggregation at synapses, probably by promoting actin polymerization. Importantly, pharmacological inhibition of the CGRP receptor *in vivo* or the silencing of its related genes (*Calcrl* or *Ramp1*) attenuated the new bone formation induced by magnesium implants (magnesium rod or Mg-IMN), whereas overexpression of *Calcrl* or *Ramp1 in vivo* enhanced the beneficial effects of magnesium implants. Of note, in addition to constituting the CGRP receptor with RAMP1, CALCRL

can also be co-expressed with RAMP2 to form a receptor for amylin, which is known to inhibit bone resorption[45]. However, gene manipulation of *Calcrl* or *Ramp1* showed similar effects on Mg-induced bone formation, which suggests the involvement of CGRP instead of amylin. Moreover, in isolated PDSCs, the key cell type involved in osteogenesis[18,20], CGRP promoted osteogenic differentiation through CGRP-receptor-coupled cAMP activation of CREB1 and SP7, transcription factors essential to osteogenesis[35,46,47]. Of note, our results both *in vitro* and *in vivo* suggest that CGRP or magnesium implant only upregulates SP7 but not RUNX2, another downstream target of CREB1 important for osteogenesis[34], which suggests the specific activation of CREB1 and SP7, leading to osteogenic differentiation (**Fig. 6d**). Further study is required to understand why RUNX2 is not responsive to magnesium or CGRP and whether other reported CREB1-regulated pathways (for example, BMP2, Wnt/β-catenin) are involved[48,49].

Taken together, these results are consistent with previous findings showing that CGRP insufficiency, accompanied by magnesium loss in the bone, is associated with delayed fracture healing in aged animals[50,51]. Sensory nerves secrete CGRP and promote callus formation and bone remodeling, whereas a lack of $CGRP^+$ nerve fibers leads to delayed union or nonunion[21,52,53]. Therefore, the presently identified role of magnesium in promoting CGRP-mediated osteogenesis has suggested its therapeutic implication in the repair of osteoporotic bone fracture or other bone diseases. Nevertheless, whether a magnesium implant or CGRP influences other cell types, such as chondrocytes, to contribute to osteogenesis awaits further investigation. It would also be important to test whether systemic administration of magnesium (such as oral pills) would promote CGRP mobilization and thus be a potential nutraceutical method for bone disorders.

A progression of the present study would be the development of a Mg-IMN system to provide both mechanical support and osteogenic benefits for repairing long-bone fracture. It is known that closed-bone fracture is commonly seen in patients with osteoporosis, the so-called low-energy osteoporotic fractures. As a proof-of-concept experiment, we used a closed-fracture model where the injury is limited to the fractured bone, with no injury to the periosteum. In addition, Mg-IMN was implanted with the drilled holes adjacent to the fracture line, ensuring that the released Mg^{2+} is delivered mostly to the wound. As expected, higher magnesium content was detected in peripheral fracture callus in the Mg-IMN group than in the IMN group. The way in which the released Mg^{2+} is transported to the periosteal region can be explained by the diameter of Mg^{2+} (<300 pm) being much smaller than that of Harversian's or Volkmann's canals within the cortical bone (in microscale level), as reported in our earlier study[54]. In addition, Mg^{2+} might diffuse through the fracture gaps (**Fig. 6d**).

The outcome seen here with Mg-IMN treatment is promising. First, Mg-IMN accelerated bone remodeling, as indicated by significant increases in callus, BV and the ratio of xylenol/calcein osteoid staining at an early stage (week 4). Second, mechanical strength is improved by Mg-IMN. At week 12, although the xylenol/calcein staining ratio is lower in the Mg-IMN group than in the IMN group, probably owing to the completion of bone remodeling, a higher BMD and better lamellar bone morphology were achieved with Mg-IMN treatment, indicating greater mechanical strength than that achieved with IMN treatment. This result is also consistent with a previous report showing better alignment of matrix collagen in Mg^{2+}-treated cells[55]. Of note, in the present study, new bone is formed mainly in the periosteal region, which, even with a small-scale increase in BV, might translate into substantial improvement in biomechanical properties (that is, bending or torsional strength), as previously reported[56,57]. Indeed, biomechanical testing confirmed a much stronger mechanical property of the bone in the Mg-IMN group at the end of experimental time frame (that is, at week 12 after implantation). In addition, the pain levels in rats with Mg-IMN treatment showed no difference relative to controls, which suggests the suitability of Mg-IMN for clinical uses.

In conclusion, the present study has revealed a CGRP-involved mechanism that underlies the osteogenic effects of magnesium-based implant. An innovative Mg-IMN system has been developed and has shown therapeutic potential for bone injuries, in particular, for the commonly seen low-energy osteoporotic fracture. With the development of specific cell or tissue targeting systems[58], it might also be possible to deliver Mg^{2+} or recombinant CGRP to specific healing sites in the bone. Therefore, the present findings could have broader implications in the treatment or prevention of other bone diseases or injuries, such as high-energy fractures resulting from sports injuries and other traumas.

METHODS

Methods and any associated references are available in the online version of the paper.

Note: Any Supplementary Information and Source Data files are available in the online version of the paper.

ACKNOWLEDGMENTS

We acknowledge Li Ka Shing Institute of Health Sciences (LiHS) for providing a harmonious working environment. This work was supported by Hong Kong RGC Collaborative Research Fund (2014/2015, C4028-14GF to L.Q.), General Research Fund (no. 14112714, 14114415 to L.Q.), NSFC/RGC (N_CUHK449/13 to L.Q.; 51361165101 to Y.Z.), Innovation and Technology Fund (no. ITS/350/13 to L.Q.), SMART Program to K.C., L.Q., H.C.C. and Y.C.R. (Lui Che Woo Institute of Innovative Medicine in Faculty of Medicine, the Chinese University of Hong Kong), National Basic Research Program of China (973 Program, no. 2012CB619102 to Y.Z., no.2012CB944903 to H.C.C. and Y.C.R. and no. 2013CB967401 to H.C.C.), National Natural Science Foundation of China (no. 51225101; no. 51431002 to Y.Z.). We thank B. Hesse for collecting and analyzing the μXRF data. We thank G. Wu and J. Lu for help with scanning electron microscopy analysis.

AUTHOR CONTRIBUTIONS

Y. Zhang, J.X., S.C., X.X., L.H., L. Zheng, S.H. and D.H.K.C. conducted animal surgery and analyzed the results. Y. Zhang, J.X., Y.C.R., and M.K.Y. conducted DRG neuron vesicles and intracellular Mg^{2+} experiments. Y. Zhang, J.X. and N.L. contributed to isolation and culture of DRG neurons and PDSCs. M.O'L. contributed to the conjugation of CGRP receptor antagonist BIBN4096BS with Cy5. L.T. and J.W. were responsible for needle design. D.S. contributed to the FEA modeling and analysis. J.Q.F., D.C., and L. Zhao (USA) performed the analysis of magnesium-implanted samples using confocal microscope. H.L. contributed to the scanning electron microscopy experiment. D.Z., K.L., and K.C. conducted the capsaicin-related experiments and provided invaluable support on the discussion about the clinical indications. H.W. and X.G. contributed to build the platform for CGRP study. F.W. (Germany) performed the synchrotron μXRF analysis. F.W. (Germany) and Y. Zheng (Beijing, China) contributed to magnesium biomedical engineering, and also provided insightful comments on the materials-science related field. H.C.C. provided intelligence input and supervision. Y.C.R drew the schematic pictures. Y. Zhang, J.X., Y.C.R. and L.Q. designed and supervised the project as well as wrote the manuscript.

COMPETING FINANCIAL INTERESTS

The authors declare no competing financial interests.

1. Cheung, W.H., Chin, W.C., Qin, L. & Leung, K.S. Low intensity pulsed ultrasound enhances fracture healing in both ovariectomy-induced osteoporotic and age-matched normal bones. *J. Orthop. Res.* **30**, 129–136 (2012).
2. Hayes, J.S. & Richards, R.G. The use of titanium and stainless steel in fracture fixation. *Expert Rev. Med. Devices* **7**, 843–853 (2010).

3. Gu, X.N., Xie, X.H., Li, N., Zheng, Y.F. & Qin, L. *In vitro* and *in vivo* studies on a Mg-Sr binary alloy system developed as a new kind of biodegradable metal. *Acta Biomater.* **8**, 2360–2374 (2012).
4. de Baaij, J.H., Hoenderop, J.G. & Bindels, R.J. Magnesium in man: implications for health and disease. *Physiol. Rev.* **95**, 1–46 (2015).
5. Li, F.Y. *et al.* Second messenger role for Mg^{2+} revealed by human T-cell immunodeficiency. *Nature* **475**, 471–476 (2011).
6. Staiger, M.P., Pietak, A.M., Huadmai, J. & Dias, G. Magnesium and its alloys as orthopedic biomaterials: a review. *Biomaterials* **27**, 1728–1734 (2006).
7. Castiglioni, S., Cazzaniga, A., Albisetti, W. & Maier, J.A. Magnesium and osteoporosis: current state of knowledge and future research directions. *Nutrients* **5**, 3022–3033 (2013).
8. Zberg, B., Uggowitzer, P.J. & Löffler, J.F. MgZnCa glasses without clinically observable hydrogen evolution for biodegradable implants. *Nat. Mater.* **8**, 887–891 (2009).
9. Witte, F. The history of biodegradable magnesium implants: a review. *Acta Biomater.* **6**, 1680–1692 (2010).
10. Witte, F. *et al. In vivo* corrosion of four magnesium alloys and the associated bone response. *Biomaterials* **26**, 3557–3563 (2005).
11. Gu, X. *et al.* Corrosion of, and cellular responses to Mg-Zn-Ca bulk metallic glasses. *Biomaterials* **31**, 1093–1103 (2010).
12. Li, H.F. *et al. In vitro* and *in vivo* studies on biodegradable CaMgZnSrYb high-entropy bulk metallic glass. *Acta Biomater.* **9**, 8561–8573 (2013).
13. Tang, J. *et al.* Surface coating reduces degradation rate of magnesium alloy developed for orthopaedic applications. *J. Orthop. Translat.* **1**, 41–48 (2013).
14. Kuhlmann, J. *et al.* Fast escape of hydrogen from gas cavities around corroding magnesium implants. *Acta Biomater.* **9**, 8714–8721 (2013).
15. Meunier, P.J. *et al.* The effects of strontium ranelate on the risk of vertebral fracture in women with postmenopausal osteoporosis. *N. Engl. J. Med.* **350**, 459–468 (2004).
16. Wang, J. *et al.* Surface modification of magnesium alloys developed for bioabsorbable orthopedic implants: a general review. *J. Biomed. Mater. Res. B Appl. Biomater.* **100**, 1691–1701 (2012).
17. Seeman, E. The periosteum—a surface for all seasons. *Osteoporos. Int.* **18**, 123–128 (2007).
18. Zebaze, R.M. *et al.* Intracortical remodelling and porosity in the distal radius and post-mortem femurs of women: a cross-sectional study. *Lancet* **375**, 1729–1736 (2010).
19. Castañeda-Corral, G. *et al.* The majority of myelinated and unmyelinated sensory nerve fibers that innervate bone express the tropomyosin receptor kinase A. *Neuroscience* **178**, 196–207 (2011).
20. Zhang, X., Awad, H.A., O'Keefe, R.J., Guldberg, R.E. & Schwarz, E.M. A perspective: engineering periosteum for structural bone graft healing. *Clin. Orthop. Relat. Res.* **466**, 1777–1787 (2008).
21. Wang, X.Y., Guo, X., Qu, S.X., Weng, J. & Cheng, C.Y. Temporal and spatial CGRP innervation in recombinant human bone morphogenetic protein induced spinal fusion in rabbits. *Spine* **34**, 2363–2368 (2009).
22. Ding, Y., Arai, M., Kondo, H. & Togari, A. Effects of capsaicin-induced sensory denervation on bone metabolism in adult rats. *Bone* **46**, 1591–1596 (2010).
23. Niedermair, T. *et al.* Absence of substance P and the sympathetic nervous system impact on bone structure and chondrocyte differentiation in an adult model of endochondral ossification. *Matrix Biol.* **38**, 22–35 (2014).
24. McDonald, A.C., Schuijers, J.A., Shen, P.J., Gundlach, A.L. & Grills, B.L. Expression of galanin and galanin receptor-1 in normal bone and during fracture repair in the rat. *Bone* **33**, 788–797 (2003).
25. Kavalali, E.T. The mechanisms and functions of spontaneous neurotransmitter release. *Nat. Rev. Neurosci.* **16**, 5–16 (2015).
26. Matteoli, M. *et al.* Differential effect of α-latrotoxin on exocytosis from small synaptic vesicles and from large dense-core vesicles containing calcitonin gene-related peptide at the frog neuromuscular junction. *Proc. Natl. Acad. Sci. USA* **85**, 7366–7370 (1988).
27. Brenner, S.L. & Korn, E.D. The effects of cytochalasins on actin polymerization and actin ATPase provide insights into the mechanism of polymerization. *J. Biol. Chem.* **255**, 841–844 (1980).
28. Feske, S., Skolnik, E.Y. & Prakriya, M. Ion channels and transporters in lymphocyte function and immunity. *Nat. Rev. Immunol.* **12**, 532–547 (2012).
29. Zhou, H. & Clapham, D.E. Mammalian MagT1 and TUSC3 are required for cellular magnesium uptake and vertebrate embryonic development. *Proc. Natl. Acad. Sci. USA* **106**, 15750–15755 (2009).
30. Goytain, A. & Quamme, G.A. Identification and characterization of a novel mammalian Mg2+ transporter with channel-like properties. *BMC Genomics* **6**, 48 (2005).
31. Chokshi, R., Fruasaha, P. & Kozak, J.A. 2-aminoethyl diphenyl borinate (2-APB) inhibits TRPM7 channels through an intracellular acidification mechanism. *Channels (Austin)* **6**, 362–369 (2012).
32. Voets, T. *et al.* TRPM6 forms the Mg^{2+} influx channel involved in intestinal and renal Mg^{2+} absorption. *J. Biol. Chem.* **279**, 19–25 (2004).
33. Zhang, Z.H. *et al.* Calcitonin gene-related peptide enhances CREB phosphorylation and attenuates tau protein phosphorylation in rat brain during focal cerebral ischemia/reperfusion. *Biomed. Pharmacother.* **64**, 430–436 (2010).
34. Nishio, Y. *et al.* Runx2-mediated regulation of the zinc finger *Osterix/Sp7* gene. *Gene* **372**, 62–70 (2006).
35. Koga, T. *et al.* NFAT and Osterix cooperatively regulate bone formation. *Nat. Med.* **11**, 880–885 (2005).
36. Fu, S.C., Cheuk, Y.C., Hung, L.K. & Chan, K.M. Limb Idleness Index (LII): a novel measurement of pain in a rat model of osteoarthritis. *Osteoarthritis Cartilage* **20**, 1409–1416 (2012).
37. Zhen, G. *et al.* Inhibition of TGF-β signaling in mesenchymal stem cells of subchondral bone attenuates osteoarthritis. *Nat. Med.* **19**, 704–712 (2013).
38. Li, J., Ahmad, T., Spetea, M., Ahmed, M. & Kreicbergs, A. Bone reinnervation after fracture: a study in the rat. *J. Bone Miner. Res.* **16**, 1505–1510 (2001).
39. Minardi, S. *et al.* Evaluation of the osteoinductive potential of a bio-inspired scaffold mimicking the osteogenic niche for bone augmentation. *Biomaterials* **62**, 128–137 (2015).
40. Weizbauer, A. *et al.* Magnesium-containing layered double hydroxides as orthopaedic implant coating materials-An *in vitro* and *in vivo* study. *J. Biomed. Mater. Res. B Appl. Biomater.* **104**, 525–531 (2016).
41. Zhao, D. *et al.* Vascularized bone grafting fixed by biodegradable magnesium screw for treating osteonecrosis of the femoral head. *Biomaterials* **81**, 84–92 (2016).
42. Chaya, A. *et al.* Fracture healing using degradable magnesium fixation plates and screws. *J. Oral Maxillofac. Surg.* **73**, 295–305 (2015).
43. Cadosch, D. *et al.* Humoral factors enhance fracture-healing and callus formation in patients with traumatic brain injury. *J. Bone Joint Surg. Am.* **91**, 282–288 (2009).
44. Boes, M. *et al.* Osteogenic effects of traumatic brain injury on experimental fracture-healing. *J. Bone Joint Surg. Am.* **88**, 738–743 (2006).
45. Naot, D. & Cornish, J. The role of peptides and receptors of the calcitonin family in the regulation of bone metabolism. *Bone* **43**, 813–818 (2008).
46. Komori, T. Signaling networks in RUNX2-dependent bone development. *J. Cell. Biochem.* **112**, 750–755 (2011).
47. Mayr, B. & Montminy, M. Transcriptional regulation by the phosphorylation-dependent factor CREB. *Nat. Rev. Mol. Cell Biol.* **2**, 599–609 (2001).
48. Tian, G., Zhang, G. & Tan, Y.H. Calcitonin gene-related peptide stimulates BMP-2 expression and the differentiation of human osteoblast-like cells in vitro. *Acta Pharmacol. Sin.* **34**, 1467–1474 (2013).
49. Mrak, E. *et al.* Calcitonin gene-related peptide (CGRP) inhibits apoptosis in human osteoblasts by β-catenin stabilization. *J. Cell. Physiol.* **225**, 701–708 (2010).
50. Rude, R.K. & Gruber, H.E. Magnesium deficiency and osteoporosis: animal and human observations. *J. Nutr. Biochem.* **15**, 710–716 (2004).
51. Madsen, J.E. *et al.* Fracture healing and callus innervation after peripheral nerve resection in rats. *Clin. Orthop. Relat. Res.* (351), 230–240 (1998).
52. Zaidi, M. Skeletal remodeling in health and disease. *Nat. Med.* **13**, 791–801 (2007).
53. Li, J., Kreicbergs, A., Bergström, J., Stark, A. & Ahmed, M. Site-specific CGRP innervation coincides with bone formation during fracture healing and modeling: A study in rat angulated tibia. *J. Orthop. Res.* **25**, 1204–1212 (2007).
54. Qin, L., Mak, A.T., Cheng, C.W., Hung, L.K. & Chan, K.M. Histomorphological study on pattern of fluid movement in cortical bone in goats. *Anat. Rec.* **255**, 380–387 (1999).
55. Xia, W. & Springer, T.A. Metal ion and ligand binding of integrin α5β1. *Proc. Natl. Acad. Sci. USA* **111**, 17863–17868 (2014).
56. Stürmer, E.K. *et al.* Standardized bending and breaking test for the normal and osteoporotic metaphyseal tibias of the rat: effect of estradiol, testosterone, and raloxifene. *J. Bone Miner. Res.* **21**, 89–96 (2006).
57. Li, X. *et al.* Targeted deletion of the sclerostin gene in mice results in increased bone formation and bone strength. *J. Bone Miner. Res.* **23**, 860–869 (2008).
58. Zhang, G. *et al.* A delivery system targeting bone formation surfaces to facilitate RNAi-based anabolic therapy. *Nat. Med.* **18**, 307–314 (2012).

ONLINE METHODS

General experimental approaches. All animal experimental protocols used in the present study were approved by the Animal Experimentation Ethics Committee of the Chinese University of Hong Kong. Sex- and age-matched animals were divided into groups randomly. No samples, rats or data points were excluded. Analyses were performed in a nonblinded fashion.

Fabrication of magnesium rod. Ultrapure (99.99%) magnesium cylindrical rods (1.28 mm in diameter, 20 mm in length) were provided by the Department of Materials Science and Engineering in Peking University (China). The magnesium rods were prepared by copper-mold injection casting under argon atmosphere using published protocol[11]. In brief, magnesium was placed in a quartz tube and melted. Then the melted magnesium was injected quickly into a copper mold, and finally, rod samples were obtained. Differential scanning calorimetry (Q100, Thermal Analysis, USA) was used to identify the thermal dynamic properties of the samples. Magnesium rods were sterilized by immersing into 70% ethanol for 30 min before implantation.

Intramedullary implantation in rat femur. Three-month-old female Sprague Dawley (SD) rats were used for surgical intramedullary implantation, as previously reported[3,12]. After the rats were anesthetized by intraperitoneal injection with ketamine (75 mg/kg) and xylazine (10 mg/kg), the right knee of the rat was exposed and a tunnel with a 1.2-mm diameter and 30 mm in length was drilled from the patellofemoral groove of the distal femur along the axis of the femoral shaft. A sterilized magnesium or stainless steel rod was inserted into the femur canal. The wound was sutured, and the rats were housed in an environmentally controlled animal-care laboratory after surgery. Serial radiographs were used to scan the operated distal femora weekly, up to week 16 after operation, for both general inspection and analysis. In some animals, BIBN4096BS (300 μg/kg body weight, Shanghai Haoyuan Chemexpress, Shanghai, China) conjugated with indodicarbocyanine (Cy5) was injected into the middle site of the right femoral shaft immediately after implantation and every other day for 2 weeks.

μX-ray fluorescence (μXRF) measurements. μXRF measurements were performed using the scanning X-ray microscope installed at beamline ID21 of the ESRF (Grenoble, France)[59]. The primary X-ray beam energy was set to 2.1 keV and focused down to a microprobe ($0.5 \times 0.8\ \mu m^2$). The flux was 2.6×10^9 photons/s. A first mirror made of Ni was used, which passes the primary energy (E1) and the third harmonic (E3) of E1 (E3/E1 intensity ratio, ~1/10). XRF and scattered radiation were collected with an energy-dispersive silicon drift detector with an active area of 80 mm^2 (XFlash 5100, Bruker, Germany), subsequently normalized by the intensity of E1. Acquisition time per point was 100 ms. The step width for collecting the XRF maps (25 adjacent lines with 5 μm spacing) was set to 5 μm. The use of the dual-energy X-ray beam configuration allowed for high excitation of magnesium and calcium with the 2.1 keV and 6.3 keV energy part of the X-ray beam, respectively. To directly compare different measurements, magnesium-to-calcium ratio was calculated from the line scans performed from the bone-marrow cavity (inside) to the periosteum (outside).

Scanning electron microscopy–energy-dispersive spectroscopy. Specimens embedded in methylmethacrylate (MMA) were sliced and polished to 100 μm in thickness for sputter coating. The elemental composition at the selected regions of interests was determined by scanning electron microscopy–energy-dispersive spectra (HITACHI SU8010; Japan).

Periosteum stripping. Under general anesthesia, the right thighs of 3-month-old female SD rats were incised from the lateral side to expose the femur bone. The muscle tissue was bluntly dissected from periosteum. Full thickness of periosteum at the region of femoral mid-shaft was stripped using sharp forceps, with partial residual attached to the peripheral cortex of the cortical bone (1/5 of the circle). The right femur with periosteum stripping was implanted with intramedullary magnesium rods from the condyle of distal femur.

Injection of $MgCl_2$ at lumbar spine. Under anesthesia, $MgCl_2$ (10 mM in 100 μl H_2O, daily, for 3 d) or same amount of saline as control was injected into the intervertebral foramen at the right lumbar levels (L3–L5) of 3-month-old female SD rats. At day 7, calcein green (5 mg/kg, Sigma-Aldrich, USA) was subcutaneously injected to label the newly formed bone. Another 7 d later, the right femora were collected and embedded for hard-tissue sectioning.

Capsaicin-induced sensory denervation. Capsaicin (Sigma-Aldrich, USA) and vehicle solution (composition of Tween-80, ethanol, saline, with volume ratio as 1:1:8) were freshly prepared before treatment. Capsaicin was sonicated in the vehicle solution until homogenously suspended. 3-month-old female SD rats were injected subcutaneously at the lumbar levels (L3–L5) with a high dose of capsaicin on 3 consecutive days (30 mg/kg on day 1, 50 mg/kg on day 2 and 70 mg/kg on day 3), according to a previously reported protocol[22]. Then, at day 4 after capsaicin injections, the rats were randomly chosen for intramedullary implantation of the magnesium rod into the distal femur.

Adenovirus-based knockdown and overexpression *in vivo*. shRNAs and full-length cDNA of rat *Calcrl* (NM_012717, encoding calcitonin receptor-like receptor) and *Ramp1* (NM_031645.1, encoding receptor activity-modifying protein 1, the binding site for CGRP) were designed according to a published protocol[60]. The shRNAs (**Supplementary Table 1**) and cDNA were synthesized by Sangon Biological Engineering Technology and Services (Shanghai, China). The plasmids of PDC316-mCMV-EGFP-cDNA-*Calcrl*, PDC316-mCMV-EGFP-cDNA-*Ramp1*, PDC316-mCMV-EGFP-shRNA-*Calcrl*, PDC316-mCMV-EGFP-shRNA-*Ramp1* and PDC316-mCMV-EGFP-NC (negative control) were generated by BioWit Technologies (Shenzhen, China). These plasmids were cloned into adenovirus vectors, and the viral-null vectors were propagated in human embryonic kidney 293 (HEK293, cat#: ATCC CRL-1573, negative for mycoplasma contamination) cells. Viral titer was determined by using standard plaque assays on HEK293 cells. The titers were set to be 1×10^{11} pfu/ml, respectively. 3 d before implantation, rats were anesthetized, and a hole (0.5-mm in diameter) in the right proximal femoral shaft was drilled for injection of the aforementioned adenoviruses (10 μl, with 10^9 pfu) into the bone-marrow cavity. The same amount of adenovirus was also injected into the surrounding periosteum.

Imaging *in vivo*. To visualize the injected Cy5-conjugated BIBN4096BS and fluorescent adenoviruses, 24 h after administration of these reagents, rats were anesthetized and shaved before chemiluminescence images were taken by an IVIS200 imaging system (Xenogen Imaging Technologies, Alameda, CA, USA)[58].

Micro-CT analysis. For nonfracture samples, rat femora were collected and implants were carefully removed before micro-CT scanning (μCT40, Scanco Medical, Brüttisellen, Switzerland), according to our established protocol[58,61]. The scan range was set to be 5 mm (300 slides) for the middle shaft. The resolution was set at 16 μm per voxel and 1024 × 1024 pixels. The region of interest (ROI) was selected from 2D images with a standardized threshold (>220) as mineralized tissue, according to the tuning. 3D reconstruction of the mineralized tissue was performed according to our established protocol[61]. A low-pass Gaussian filter (Sigma = 1.2, Support = 2) was used for 3D reconstruction. Quantitative analysis involved all 300 slides of the 2D images. Morphometric parameters included total TV, BV, BV/TV and ρMOI.

For fracture samples, Mg-IMN or IMN was removed carefully, and femoral samples were wrapped in wet gauze and fitted in the sample tube (Ø 38 mm) for micro-CT scanning (μCT40, Scanco Medical, Brttisellen, Switzerland), as we previously reported[61]. In brief, the scan range was set as 10 mm (650 slides), and the fracture line was set in the middle site of this range. The resolution was set to be 16 μm/voxel and 1024 × 1024 pixels. ROI was selected from 2D images with a standardized threshold (>165) as mineralized tissue. 3D reconstruction of the mineralized tissue was performed with a low-pass Gaussian filter (Sigma = 1.2, Support = 2). Quantitative analysis included all 650 slides of 2D images.

Histological and histomorphometric analysis. After micro-CT scanning, samples were decalcified in 15% ethylene diamine tetraacetic acid (EDTA) for 10 weeks before they were embedded in paraffin, after dehydration in a series of ethanol and xylene. Sections with a thickness of 6 μm were cut and subjected to H&E and safranin O staining for the evaluation of newly formed bone under light microscope (ZEISS AxioPlan2, Germany). Immunohistochemical and

doi:10.1038/nm.4162

immunofluorescence staining was used for determining the expression of CGRP. Rabbit polyclonal antibody to CGRP was purchased from Abcam (ab47027, working with a dilution of 1:200).

The sequential fluorescence labeling was used to evaluate new-bone formation rate or bone remodeling during fracture healing, as we previously reported[58,61]. Calcein green (5 mg/kg, Sigma-Aldrich, USA) was subcutaneously injected into rat femora 7 d before xylenol orange (90 mg/kg, Sigma-Aldrich, USA) was injected in the same way. Another 7 d afterwards, rats were sacrificed, and femora were collected and embedded in MMA without decalcification and sectioned into thick sections (200 μm). The tissue sections were further ground and polished to 100 μm for the evaluation of new-bone formation rate under a fluorescence microscope (Leica Q500MC, Leica, Germany). To calculate the temporal change of new bone formation, 5 mm proximal and 5 mm distal to the fracture line was chosen as the ROI for quantification of new bone formation. The ratio of area labeled with xylenol orange to area labeled with calcein green was determined using ImageJ.

Fracture callus was digitalized under light microscope (Zeiss, Germany) and then quantified by ImageJ for bone-tissue-area fraction and cartilage-tissue-area fraction. A polarized light microscope was also applied to analyze the collagen birefringence arrangement in decalcified sections.

Detection of neuropeptides by ELISA. The femora of the rats with and without magnesium implantation were harvested, and the mid-shaft of 1 cm in length was prepared for ceramic morta, ground into mud before putting into 15-ml plastic tubes. Pre-cool lysis buffer (1 ml, with 1M hydrochloric acid) was added into the tube and put into the ice bath. After oscillation and homogenization for 1 h, the buffer was transferred into a 1.5-ml tube and centrifuged at 12,000 rpm for 30 min. The supernatant was collected for BCA protein quantitative analysis, and 200 μl of supernatant from each specimen was used for the quantitative detection of CGRP (Elabscience Biotechnology, USA), substance P, neurokinin K and galanin (LifeSpan Bioscience, USA) by ELISA kit. The ELISA result was normalized by the concentration of total protein for each specimen.

Detection of CGRP expression in dorsal root ganglions. The right DRGs at lumbar L4 of SD rats were isolated according to a published procedure[62]. Briefly, after the administration of an overdose of phenobarbital, laminectomy was performed to remove the vertebral canal roof and to expose DRGs and the spinal cord. The isolated L4 DRG was transferred into a tube with 10 ml of PBS (containing 10% penicillin-streptomycin-neomycin (PSN), from Life Technologies) without Ca^{2+}/Mg^{2+}. After fixation in 4% formalin solution for 24 h, the DRGs were dehydrated in 30%-sucrose solution. Cryosections (10-μm thick) were prepared for immunofluorescence staining of CGRP (Abcam, ab47027, 1:200).

Primary culture of DRG neurons. We isolated sensory neurons from L3–L5 DRGs by sequential digestion using papain, type I collagenase (1 mg/ml) and 0.25% trypsin solutions by following reported protocols[62–64]. Morphologically distinct phase-bright neurons (50%) and phase-dark glial cells (50%) were observed right after isolation. These isolated cells were re-suspended in F12 medium and plated on round-glass slices (2.5 cm in diameter) coated with laminin (20 ng/ml, Life Technologies) and poly-D-lysine hydrobromide (50 ng/ml, Life Technologies) at a density of 5,000 cells/ml. 4 h after plating, the culture medium was replaced with F12 medium containing 10% FBS, 1% PSN, 20 ng/ml NGF (Sigma-Aldrich, USA), 10^{-5} M fluorodeoxyuridine (Sigma-Aldrich, USA) and 10^{-5} M uridine (Sigma-Aldrich, USA) for another 72 h in incubation, before the large phase-bright DRG neurons were used for further tests.

Detection of synaptic vesicles in DRG neurons. We used fluorescent dye FM1-43 (N-(3- triethylammoniumpropyl)-4-(4-(dibutylamino)styryl) pyridinium dibromide) (Biotium, Hayward, USA) to label and trace the change and movement of synaptic vesicles in live DRG neurons, as previously reported[65]. The isolated DRG neurons were seeded on cover glasses. On the experimental day, the cells were washed twice with a high K^+ and Mg^{2+}-free (HKMF) Margo's solution containing (in mM): 45 NaCl, 90 KCl, 2.5 $CaCl_2$, 20 HEPES acid and 10 glucose, before incubation with FM1-43 (10 μM) in HKMF Margo's at 37 °C for 15 min. Afterwards, cells were washed with Mg^{2+}-free Margo's solution containing (in mM): 130 NaCl, 5 KCl, 2.5 $CaCl_2$, 20 HEPES acid and 10 glucose, for three times before being transferred to a mini-chamber and mounted to a confocal microscope (Zeiss, Germany). $MgCl_2$ (1–2 mM) or NMDG-Cl (2–4 mM) as a control was added to the Mg^{2+}-free Margo's bath in the presence or absence of cytochalasin B (20 μM). Z-stack (0.8–1 μm intervals) confocal images of the DRG neurons were captured every 2–10 min. The Z-stack series was projected into a single image for each time-point capture by the software Exciter (Carl Zesis, Germany), the fluorescence intensity of which was analyzed and quantified by the software ImageJ (version 1.42q, NIH, USA).

Measurement of intracellular Mg^{2+} in DRG neurons. DRG neurons were seeded on cover glasses 72 h before the experiments. The cells were incubated in the Mg^{2+}-free Margo's solution supplemented with 2 μM Mg-Fura2 (Life Technologies, USA) and 1 μM Pluronic F-127 (Life Technologies, USA) for 30 min before being washed with the Mg^{2+}-free Margo's solution and stabilized for another 30 min at room temperature. After the cells were transferred to a mini-chamber that was mounted to a microscope (Nikon Eclipse Ti, Japan) equipped with a CCD camera (Spot Xplorer, USA) and a Fluor 20X objective lens (0.75 NA, Nikon, Japan), Mg-Fura2 was excited at 340 nm and 380 nm, respectively. Fluorescence signals were monitored, and pictures were taken every 5 s by a microscope (Nikon Eclipse Ti, Japan). The fluorescence ratio was measured by the software MetaFluor (USA).

ATP assay. ATP concentrations were determined using a luminescence ATP-detection assay system (ATPLite, PerkinElmer, USA), according to the manufacturer's guidelines.

2,5-fluorescein isothiocyanate (FITC) staining for confocal imaging. FITC-stained samples were prepared according to our established protocol[66]. In brief, rat femora were fixed and dehydrated and then 1% FITC (Sigma-Aldrich, USA, cat. #F7250) in 100% ethanol was used to immerse the samples overnight. The samples were further dehydrated with 100% ethanol and acetone, followed by plastic embedding and sectioning. The SP5 Leica confocal microscope was used to gather stackable images.

Isolation and culture of rat PDSCs. Femora of 1-month-old female rats were collected, and periosteum from mid-shaft to distal femur was collected and put into Dulbecco's Modified Eagle's Medium (DMEM) supplemented with 10% FBS and type I collagenase (1 mg/ml). The periosteum was digested in a 37 °C incubator for another 8 h, and the filtered medium was centrifuged (1,000*g* for 5 min) to collect the periosteal cells. The mixed cells were plated at an optimal low-cell density (1,000 cells/cm^2) in a humidified atmosphere at 37 °C, 5% CO_2 to form colonies. At day 2 after initial plating, the cells were washed twice with PBS to remove nonadherent cells. At days 7–10, large round colonies (>200 cells) were trypsinized and mixed together as passage 1. The collected cells were subcultured after reaching 80–90% confluence. Cells at passage 3–5 were used for further experiments.

Fluorescence staining for stem cell markers. PDSCs were seeded on glass slides at a density of 10,000 cells/slide and cultured for 24 h. After the cells were fixed and blocked with 5% BSA solution for 1 h, the monoclonal rabbit anti-rat primary antibody to CD44 (Abcam, ab24504), CD90 (Abcam, ab92574) and CD105 (Abcam, ab107095) were incubated with cells with a dilution of 1:500 (v/v) at 4 °C overnight. After washing with PBS twice, Cy5-conjugated goat anti-rabbit secondary antibody with a dilution of 1:1,000 was applied to the slides for 1 h. The cells were washed in PBS, counterstained with DAPI and examined by a fluorescence microscope (Leica Q500MC, Leica, Germany).

Cell proliferation assay. PDSCs or MC3T3-E1 clone 4 cell line (ATCC CRL-2593, negative for mycoplasma contamination) were plated at a density of 4,000 cells/cm^2 in a 96-well plate and incubated in a 37 °C incubator with supplementation of 5% CO_2. Cell proliferation was assessed using MTT assay (Sigma-Aldrich, USA) at days 1, 2 and 3. The absorbance at 570 nm was measured and reported[67]. 10^{-16} to 10^{-8} M CGRP (Abcam, USA, cat. #ab47101) was used.

Real-time PCR. PDSCs were plated at a density of 4,000 cells/cm^2 in a 12-well plate and cultured in basal culture medium until 90% confluence. High-glucose

DMEM supplemented with 10% FBS, 1 nM dexamethasone, 50 μM ascorbic acid, and 20 mM β-glycerolphosphate (the last three chemicals were from Sigma-Aldrich, USA) was used as osteogenic induction medium. At day 14 after osteogenic induction, PDSCs were harvested and homogenized for RNA extraction using the RNeasy mini kit (Qiagen, Germany)[58]. Total mRNA was reverse-transcribed to cDNA using the First Strand cDNA kit (Takara, DaLian, China). Then, 1 μl of total cDNA of each sample was amplified in a 10-μl reaction system (for 384-well plate) containing the SYBR Green qPCR SuperMix-UDG and specific primers (**Supplementary Table 2**) for *Opn*, *Bglap*, *Alp* and *Actb* using the ABI 7900HT real-time PCR system (Applied Biosystems, USA). The expression of the target gene was normalized to that of *Actb*. Relative gene expression was calculated using the $2^{-\Delta CT}$ formula.

Alizarin red and ALP staining assay. PDSCs were plated at 4,000 cells/cm^2 in a 12-well plate and cultured in complete medium until confluence. At day 14 after osteogenic induction, the cells were fixed for AR and ALP staining (Sigma-Aldrich, USA) and subsequent imaging evaluation using HP Scanjet G3110 Photo Scanner, as described previously[67].

Western blotting. Specific primary antibodies against CALCRL (Abcam, ab83697), RAMP1 (Abcam, ab203282), RUNX2 (Abcam, ab76956), SP7 (Abcam, ab94744), pCREB1 (Abcam, ab32096) and β-actin (Abcam, ab8227) were diluted to 1:1,000 (v/v) in blocking buffer for incubation of the membranes overnight, respectively. After incubating with HRP-labeled secondary antibodies against the species of primary antibodies under a dilution of 1:8,000 (v/v) for 1 h at room temperature, HRP signals were detected using an enhanced chemiluminescence kit (Amersham Biosciences, USA).

Conditioned medium from the DRG neurons. Isolated DRG neurons were seeded onto 6-well plates at a density of 10,000 cells/cm^2. Once fully attached, DRG neurons were cultured in growth medium (containing 1 mM of Mg^{2+}) supplemented with additional $MgCl_2$ (1 mM) or NaCl (2 mM) as a control for 72 h, after which 2 ml of medium from each well was collected and concentrated by a column (Millipore) into a final volume of 100 μl. The concentrates were diluted at 1:100 with osteogenic induction medium and used for osteogenic differentiation of PDSCs.

Design of the magnesium-containing intramedullary nail (Mg-IMN). Hollow spinal needles (18 G, with an outer diameter of 1.27 mm and an inner diameter of 0.9 mm) were purchased from Terumo (Terumo, USA). Holes were drilled by electric sparks burning in vertical directions at the transverse section with an equal distance of 0.5 mm by Ziyoujian (Shenzhen, China). Afterward, an ultrapure magnesium rod was inserted into the needles. In the finite elemental analysis (FEA) analysis, 10-node tetrahedron element, SOLID 92, was chosen to mesh the needle in ANSYS (ANSYS, Canonsburgh, PA, USA). The size of the mesh element was 0.05 mm. The mechanical properties of the needle (modulus as 210 GPa, poison ratio as 0.3) were input into the software. A parallel vertical force of 20 N at each loading point was applied downwardly to the needle.

Establishment of closed-fracture model in osteoporotic rats. 6-month-old female rats were used to establish standard ovariectomy-induced osteoporosis model, according to our well-established protocols[1,68]. Closed femoral fracture was established on the right femur of rat, according to our published protocol[1]. The rats were randomly divided into Mg-IMN and IMN groups. Mg-IMN or IMN was inserted into the fractured femur along its vertical axis from the patellofemoral groove to the greater trochanter. Analgesia was given every day for 3 d after surgery for pain relief.

Measurement of nerve sprouting. Primary antibodies for GAP-43 (Abcam, ab16053, 1:1,000) and PGP-9.5 (Abcam, ab8189, 1:1,000) were purchased from Abcam. At day 4, day 7 and day 14 after fixation, bone specimens 5 mm above and below the fracture line were collected for protein extraction and measurement of GAP-43 and PGP9.5 expression by western blotting, as described above.

Radiographic analysis of fracture callus. The radiographs were analyzed according to our established protocol[61]. Radiographic healing was defined as complete bridging of the mineralized callus. Callus width (CW) was defined as the maximum width of callus, and callus area (CA) was equal to the size of radiopaque area of callus as shown in the radiographs. Both CW and CA were measured on a lateral radiograph of each rat by using ImageJ. The measurement for each callus was repeated three times, and the average was used for statistical analysis.

Biomechanical test. Four-point bending test was performed for evaluating the fracture-healing quality using a mechanical testing machine (H25KS Hounsfield Test Equipment, Redhill, Surrey, UK), as described in our previous study[61]. In brief, the femora were placed with the anterior–posterior direction on the lower supporting bars at 26 mm apart, and the upper bars at 10 mm apart, flanking the fracture callus. A compression load was applied at a compression speed of 5 mm/min until failure. The maximum compressive load was derived from the load-deformation curve in built-in QMAT software (Redhill, Surrey, UK).

Gait analysis for pain measurement. Automated gait analysis was performed before surgery as a baseline, 1 week and 2 weeks after surgery, using a CatWalk system (Noldus, Wageningen, Netherlands), as previously described[36,37]. Briefly, we trained the rats to cross the CatWalk walkway daily for 2 d before the implantation of magnesium or stainless steel. After setting the thresholds to pick up the illuminated contact prints, each rat was placed individually in the CatWalk walkway. The rats were allowed to walk freely. Video recording of paw prints was automatically triggered when the rats entered the ROI. Recorded runs with a steady walking speed (variation, < 30%) were accepted as compliant runs for paw-print auto-classification as left forelimb (LF), right forelimb (RF), left hind limb (LH) and right hind limb (RH) by the built-in software. After checking the correctness of classification manually, we only further analyzed the runs with normal alternate footfall pattern (LF→RH→RF→LH). Limb idleness index, another parameter for the assessment of pain[36], was calculated from the raw data. Animals for pain test were not given analgesia.

Statistical analysis. Sample size was based on preliminary data as well as on observed effect sizes. Data are presented as means ± s.e.m., with *n* as the number of tissue preparations, cells or animals. Unpaired or paired two-tailed Student's *t* test was used for comparison between two groups. Data distribution was previously tested with the Shapiro–Wilk test. One-way or two-way ANOVA with relevant *post hoc* tests was used for multiple-group comparisons. Box-and-whisker plots were used to describe the entire population without assumptions about the statistical distribution. $P < 0.05$ was considered to be statistically significant. GraphPad Prism software (Version 6.01) was used for above statistical analysis.

59. Salomé, M. *et al.* The ID21 scanning X-ray microscope at ESRF. *J. Phys. Conf. Ser.* **425**, 182004 (2013).
60. Tian, S.F. *et al.* Mechanisms of neuroprotection from hypoxia-ischemia (HI) brain injury by up-regulation of cytoglobin (CYGB) in a neonatal rat model. *J. Biol. Chem.* **288**, 15988–16003 (2013).
61. Suen, P.K. *et al.* Sclerostin monoclonal antibody enhanced bone fracture healing in an open osteotomy model in rats. *J. Orthop. Res.* **32**, 997–1005 (2014).
62. Zheng, L.F. *et al.* Calcitonin gene-related peptide dynamics in rat dorsal root ganglia and spinal cord following different sciatic nerve injuries. *Brain Res.* **1187**, 20–32 (2008).
63. Ng, K.Y., Wong, Y.H. & Wise, H. Glial cells isolated from dorsal root ganglia express prostaglandin E(2) (EP(4)) and prostacyclin (IP) receptors. *Eur. J. Pharmacol.* **661**, 42–48 (2011).
64. Ng, K.Y., Yeung, B.H., Wong, Y.H. & Wise, H. Isolated dorsal root ganglion neurones inhibit receptor-dependent adenylyl cyclase activity in associated glial cells. *Br. J. Pharmacol.* **168**, 746–760 (2013).
65. Henkel, A.W., Lübke, J. & Betz, W.J. FM1-43 dye ultrastructural localization in and release from frog motor nerve terminals. *Proc. Natl. Acad. Sci. USA* **93**, 1918–1923 (1996).
66. Ren, Y., Lin, S., Jing, Y., Dechow, P.C. & Feng, J.Q. A novel way to statistically analyze morphologic changes in Dmp1-null osteocytes. *Connect. Tissue Res.* **55** Suppl 1, 129–133 (2014).
67. Xu, J.K. *et al.* Optimal intensity shock wave promotes the adhesion and migration of rat osteoblasts via integrin β1-mediated expression of phosphorylated focal adhesion kinase. *J. Biol. Chem.* **287**, 26200–26212 (2012).
68. He, Y.X. *et al.* Impaired bone healing pattern in mice with ovariectomy-induced osteoporosis: A drill-hole defect model. *Bone* **48**, 1388–1400 (2011).

doi:10.1038/nm.4162